

# Source mechanisms of laboratory earthquakes during fault nucleation and formation

Thomas King<sup>1,2\*</sup>, Sergio Vinciguerra<sup>1</sup>, Jodi Burgess<sup>3</sup>, Philip Benson<sup>3</sup> and Luca De Siena<sup>4,5</sup>

<sup>1</sup> Department of Earth Sciences, University of Turin, Via Tommaso Valperga Caluso, 35, 10125 Turin, Italy; thomas.king@edu.unito.it; sergiocarmelo.vinciguerra@unito.it

<sup>2</sup> Istituto Nazionale di Geofisica e Vulcanologia, Sezione di Catania - Osservatorio Etneo, Catania, Italy

<sup>3</sup> Rock Mechanics Laboratory, School of Earth and Environmental Sciences, University of Portsmouth, Burnaby Building, Portsmouth PO1 3QL, UK; philip.benson@port.ac.uk

<sup>4</sup> Institute of Geosciences, Johannes Gutenberg University, Mainz, Germany; ldesiena@uni-mainz.de

<sup>5</sup> Department of Geology and Petroleum Geology, School of Geosciences, University of Aberdeen, King's College, Aberdeen AB24 3FX, UK;

\* Corresponding author: thomas.king@ingv.it

## ABSTRACT

Identifying deformation and pre-failure mechanisms preceding faulting is key for fault mechanics and for interpreting precursors to fault rupture. This study presents the results of a new and robust derivation of first motion polarity focal mechanism solutions (FMS) applied to Acoustic Emission (AE). FMS are solved using a least squares minimisation of the fit between projected polarity measurements and the deviatoric stress field induced by dilatational (T-type), shearing (S-type) and compressional (C-type) sources. 4x10 cm cylindrical samples of Alzo Granite (AG, porosity <1%) and Darley Dale Sandstone (DDS, porosity ≈14%) underwent conventional triaxial tests in order to investigate the relationships between increasing confining pressure (5,10,20 and 40 MPa), deformation and failure mode, and role of microstructural features. Results highlight that S-type events occur in very low numbers with poor spatial correlation to fault structure. Instead, deformation is driven by a complex interplay between

28 compactant (C-type) and dilatant (T-type) regions of deformation. C-type events are the earliest  
29 precursor related to crack nucleation and T-type events mark new cracks opening, with the onset  
30 of fracture growth characterised by periodic cycles of coalescence. For AG a single sequence is  
31 able to lead to dynamic failure, while for DDS several cycles are needed for coalescence to take  
32 place due to the competition between dilatant and compactant deforming regions induced by  
33 multiple fracture nucleation sites. The occurrence of C- and S-type events is also consistent with  
34 a quasi-static premonitory phase, or foreshock, before a critical nucleation length allows the  
35 development of a planar localization.

## 36 **1 INTRODUCTION**

37 Seismic data provides key information on the physics of the fracture process ranging from  
38 fracture nucleation, crack growth and damage accumulation, to crack coalescence and strain  
39 localisation. Several micromechanical models have been developed over the years which seek to  
40 describe failure modes (e.g. Ashby and Hallam, 1986; Kemeny and Cook, 1991), taking into  
41 account pore-emanant fracturing (Baud et al., 2014), sliding wing cracks (Baud et al., 2014),  
42 friction effects (McClintock, 1962) and pore collapse (Zhu et al., 2010). To link these models to  
43 geophysical signatures recorded at the field scale, controlled laboratory rock deformation  
44 experiments equipped with dense microseismic arrays have become a routinely used tool (e.g.  
45 Locker et al., 1991; Benson et al., 2007; Fazio et al., 2017). Here, fault growth may be  
46 considered analogous to the field scale development of earthquake rupture generating Acoustic  
47 Emission (AE), which is a well-used analogue to tectonic earthquakes due to the scale invariance  
48 of these processes (Hanks, 1992; Hatton et al., 1994; Hudson and Kennett, 1981). The inclusion  
49 of AE sensors are now a routine laboratory rock physics method in the investigation of fault zone  
50 structure with the added benefit of a controlled environment.

51        There is an extensive literature reporting the evolution of fracture mechanisms inferred from  
52 the analysis of AE (e.g. tensile, shear or compaction) that occur as damage propagates (e.g.  
53 Stanchits et al., 2006; Zang et al., 1998). Triaxial rock deformation experiments on fine-grained  
54 granites suggest that this process is tensile dominated (Cox and Scholz, 1988), whereas a higher  
55 proportion of shear-components are found in coarser-grained materials (Lei et al., 1992). This  
56 hypothesis is further supported by new observations linking macroscopic shear fracture to  
57 microcrack development prior to the yield point (Lei et al., 2000), highlighting the occurrence of  
58 tensile fracturing at the front of a shear process zone. These scenarios can be described as either  
59 strongly cohesive, where intergranular boundaries have little impact, or weakly cohesive, where  
60 such boundaries are easily ruptured by applied stresses (Baud et al., 2014).

61        The fracturing process is often described as a series of localised clusters of ‘damage’ that  
62 accumulate through time (Kádár et al., 2020). These nucleating fractures amplify local stress  
63 concentrations, allowing for new fractures to further develop and grow in proximity.  
64 Furthermore, pre-existing flaws such cracks and pores concentrate stress, further promoting the  
65 development of a shear plane. (Healy et al., 2006; McBeck et al., 2019). This ‘excitation’ of fault  
66 growth, where the propagation of fractures encourages the development of secondary cracks in  
67 the vicinity is an important aspect of fault zone formation (Chen et al., 2014). The density and  
68 distribution of initial flaws, which control material cohesion and the elastic strain in the lead-up  
69 to failure, thus plays a critical role in determining when and how a rock will fail.

70        The aim of this study is to identify damage indicators in the fracture development process by  
71 mapping rupture source mechanisms (tensile, shear, collapse) derived from microseismic  
72 signatures (AE) recorded during conventional triaxial deformation experiments. Two lithologies,  
73 representing end members in terms of rock physical properties (e.g. fabric, porosity, grain size,

74 cementation), were used: Alzo Granite (AG), Italy and Darley Dale Sandstone (DDS), United  
75 Kingdom. Unlike the commonly used average polarity method (e.g. Stanchits et al., 2006) the  
76 approach reported here uses the source radiation pattern (Finck et al., 2003; Kwiatek and Ben-  
77 Zion, 2013) to categorise events and obtain source orientations of mixed-mode type mechanisms.

## 78 **2 DATA AND METHODS**

### 79 ***2.1 MATERIALS INVESTIGATED AND SAMPLE PREPARATION***

80 Alzo granite (AG) is typical of the white granites found in North-Western Italy. It is a  
81 medium-grained, plutonic rock comprising quartz, feldspar and a high biotite content. Crystal  
82 sizes range between 2.5-6 mm for the biotite and 4-9 mm for the quartz and feldspars. Porosity  
83 (water immersion method) values are characteristically low at  $0.72\% \pm 0.1\%$  (Bugini et al.,  
84 2000). Cavallo et al. (2004) report an unconfined compressive strength of 229 MPa. Conversely,  
85 Darley Dale sandstone (DDS) from the quarry of Darley Dale, Derbyshire, U.K. is a brown-  
86 yellow, feldspathic sandstone with a modal composition of quartz (69%), feldspars (26%), clay  
87 (3%) and mica (2%). Previous studies report a connected porosity (water immersion method) of  
88  $13.3\% \pm 0.8\%$  with grain sizes varying from 100-800  $\mu\text{m}$  (Heap et al., 2009; Zhu and Wong,  
89 1997). The unconfined compressive strength is approximately 160 MPa (Baud and Meredith,  
90 1997). At the scale analysed here, no distinct layering or laminations were present. Cylindrical  
91 rock samples were cored using a diamond tipped hollow coring drill to prepare 40mm diameter  
92 samples that were then trimmed to 100 mm length with a diamond saw. End faces are accurately  
93 ground using a lathe fitted with a cross-cutting diamond grinding disk with surfaces flat and  
94 parallel to within 0.01 mm.

95 **2.2 LABORATORY METHODS**

96 Experiments were undertaken using a conventional triaxial apparatus (Sanchez  
 97 Technologies), installed at the University of Portsmouth, UK (Benson et al., 2019). Laboratory  
 98 acquisition parameters are summarised in **Table 1**. The apparatus is designed to deform  
 99 cylindrical samples of 40 x 100 mm specimens at confining pressures of up to 100 MPa. A high  
 100 flash-point oil (270°C) is used as a confining medium and provides confining pressure ( $\sigma_2 = \sigma_3$ )  
 101 via 100 MPa precision piston pump. Axial stress ( $\sigma_1$ ) is applied via a hydraulic  
 102 intensifier/booster assembly that translates fluid pressure from a second syringe pump to a  
 103 maximum stress of 680 MPa across a 40mm sample diameter. As confining pressure increases to  
 104 the target level, axial stress is increased via digital servo control to maintain isostatic conditions.  
 105 Once the desired environmental setting is achieved, the experiment begins with axial strain  
 106 increased at a constant deformation rate of 3.6 mm/hr.

107 Table 1: Summary of laboratory acquisition parameters.

Characteristic	Value
<b>Experimental Conditions</b>	
Confining Pressure	5, 10, 20 and 40 MPa
Deformation Rate	3.6 mm/hr
Sample Dimensions	40 x 100 mm
Sample Shape	Cylinder
<b>Data Acquisition</b>	
Sensor Model	PAC Nano30
Frequency Sensitivity	1 MHz
Flat Frequency Response	125 - 750 KHz
No. of Sensors	12
Trigger Voltage	100 mV
Preamplifier	40 dB

108 Axial displacement is measured with a non-contact Eddy Displacement System (EDS)  
 109 attached to the apparatus. They are external to the pressure chamber and comprise of three

110 sensors mounted to a lower fixed ring. The transducers accurately (sub-micron) record axial  
111 displacement by measuring the response from a target steel plate, which is attached to the top  
112 piston and responds with sample strain. Three readings are averaged and used to calculate strain,  
113 setting a target deformation rate via feedback to the axial stress intensifier. Strain values are  
114 subsequently corrected for machine stiffness (Fazio, 2017). Each sample was positioned inside  
115 an engineered rubber jacket fitted with ports where an array of twelve 1 MHz single-component  
116 Piezo-Electric Transducers (PZTs, model PAC Nano30) were embedded (e.g. Benson et al.,  
117 2007). These sensors have a relatively flat frequency response between 125-750 KHz. Sensor  
118 output is connected to preamplifiers (selectable between 30-70dB) and split between two AE  
119 recorders. One output is used for continuous digitization, and a second recorder operates in a  
120 standard “triggered” mode which downloads all 12 channels when any single channel passes a  
121 set 100mV threshold. Both systems used an amplification of 40dB for the experiments presented  
122 here, which also include a band-pass filter of 10 kHz to 1 MHz to remove local noise which  
123 prioritised AE data quality over large numbers of events (Fazio et al., 2017); however, only the  
124 triggered mode data is used in this study. In addition to passive mode (recording fracture events  
125 across the array), the sensors may be used in ‘active’ mode for P-wave elastic velocity  
126 measurements. To generate a survey, each sensor was triggered in sequence with a high voltage  
127 (200V) pulse; the energy was recorded by the remaining 11 sensors in the array. Signal-to-noise  
128 was further improved by pulsing each sensor multiple times (16) and stacking the received  
129 waveforms, with each survey of 12-sensors generating 144 raypaths and taking approximately 30  
130 seconds to complete. Velocity surveys were performed periodically through the experiment in  
131 order to derive velocity models for source location.

## 132 **2.3 COMPUTATIONAL METHODS**

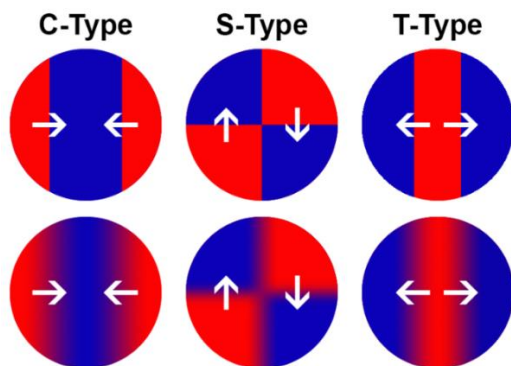
133 The onset of recorded AE are picked automatically using a Distributed Time Delay Neural  
134 Network (King et al., 2020; Peddinti et al., 2015; Waibel et al., 1995). A model is trained on  
135 timeseries of instantaneous frequency (Huang et al., 1998), seismic amplitude and permutation  
136 entropy (Unakafova and Keller, 2013). By applying a simple binary classification to each AE  
137 signal, the waveform is categorised as either “background noise” or “signal”. A simple Time  
138 Difference of Arrival method (TDOA) is applied to locate the AE epicentres using the onset time  
139 of the “signal” classification (Comanducci et al., 2020; Tobias, 1976). Finally, pairwise  
140 subtraction of observed arrival times (a minimum of 6) to each sensor are minimised against  
141 calculated arrivals times through iterative estimation of the source location. The process is  
142 repeated until the location residual arrives to a local minimum, at the true source location.

143 Measurement of first motion polarity is as follows; each waveform of a located AE event is  
144 lowpass filtered to remove high frequency noise and the root mean square envelope is calculated  
145 (smoothing = 5). Starting from the onset of energy, the first motion is selected when amplitudes  
146 exceed 1.1 times the pre-signal noise and the signal begins to decrease in amplitude, thus  
147 targeting the first oscillation of the waveform. Polarity amplitudes for each event are then  
148 normalised to the maximum arrival amplitude of that event and projected onto a sphere (using a  
149 minimum of 8 measurements).

150 The objective of the following procedure is to minimise the fit between idealised focal  
151 spheres of tensile (T-type), shearing (S-type) and compaction (C-type) events and iterative  
152 rotation (azimuth and elevation) of measured values (**Figure 1**). Idealised spheres are segmented  
153 according to those of Finck et al., (2003), where T-type represents dominantly dilatational or

154 mixed-mode fracturing, and S-type as a pure double-couple source. C-type mechanisms are  
155 considered as a compensated linear vector dipole or CLVD source. As the geometry of the  
156 radiation pattern is inverse to T-type, C-type events are considered to be dominantly  
157 compressional in this study.

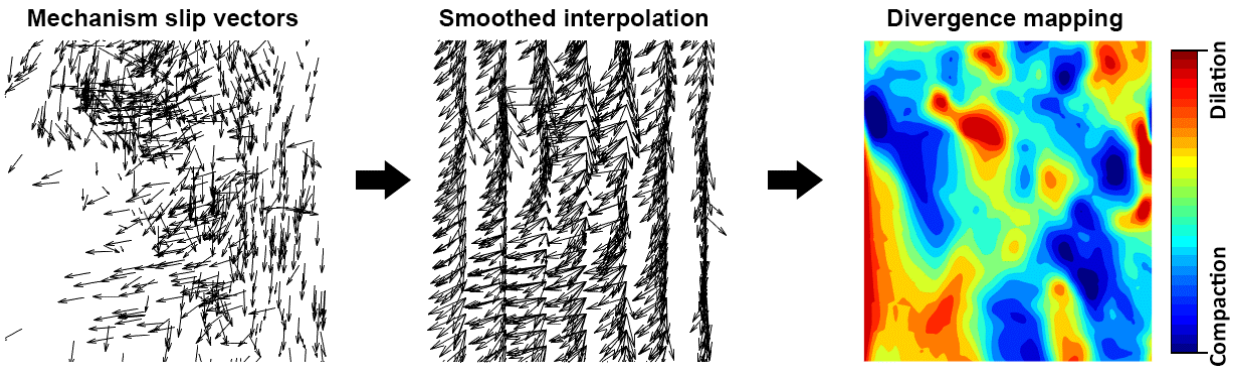
158 The minimisation constant is defined as the multiplication of the L2 norm of absolute  
159 polarity residuals (-1 or 1 - **Figure 1a**) and the L2 norm of deviatoric amplitude residuals  
160 (smoothed distribution - **Figure 1b**). This value arrives to a minimum at the best-fitting  
161 orientation of measured polarities. This method is applied for each idealised sphere and the one  
162 with the lowest minimisation constant is selected as the true mechanism category. Slip planes are  
163 estimated from solved focal mechanisms. Estimated orientation of a focal ‘plane’ is derived from  
164 the direction of motion. For C-type events, this is perpendicular to motion, whilst for S-type and  
165 T-type it is assumed parallel. Either plane may be selected for S-type events, however, under the  
166 compressive conditions of these experiments, normal (shear) faulting parallel to the shear  
167 direction is assumed.



168  
169 Figure 1: Absolute polarity (above) of idealised focal mechanisms of C-type (left), S-type (middle) and T-type  
170 (right) fracturing. Deviatoric amplitude distribution of the same mechanisms (below). White arrows indicate  
171 direction of motion from dilatant (red) to compactant (blue) regions.

172 This iterative method has some limitations. The first is associated to the choice of  
173 segmentation of the idealised focal spheres. Fracturing mechanisms fall within a range of  
174 distributions whose extremes are pure compaction, pure shear and pure tension (Frohlich et al.,  
175 2016). Unlike moment tensor inversion (e.g. Vavryčuk, 2005), our approach is limited to specific  
176 motions and is thus unable to precisely identify the amount of shear in a tensile event. Recent  
177 studies have highlighted the importance of regions of dilatancy and compaction in X-ray  
178 tomography during fault formation (Renard et al., 2019). By targeting specific fracturing  
179 mechanisms through the segmentation, variations of dilation and compaction in fracturing can be  
180 better studied. Attenuation or other scattering effects of the recorded waveforms are not  
181 accounted for here, which may affect the goodness of fit to the deviatoric mechanism (Vavryčuk,  
182 2005). Furthermore, there is an increased uncertainty for events located above and below the  
183 sensing array due to poor azimuthal coverage of those events. As the majority of events are  
184 located in the centre of the samples, where fracturing is generally diffuse, attenuation and  
185 scattering effects are considered to have a minimal impact on overall trends in the data.

186 To calculate the slip vectors, azimuthal directions are normalised according to the modal  
187 direction of S-type events for each experiment as these AE were principally orientated according  
188 to the dip direction of the fault zone. This allows to separate out events that dip parallel to the  
189 macroscopic failure plane from those that dip perpendicular to it. Given a dominance of shear  
190 faulting under compressive conditions, fracture azimuth and dip are assumed as slip vectors in  
191 order to calculate the divergence between neighbouring events. Vector directions are interpolated  
192 onto a 3D grid to identify general trends in stress orientation, after which the along-strike  
193 component is set to zero to calculate vector divergence as a 2D plane (**Figure 2**).



194

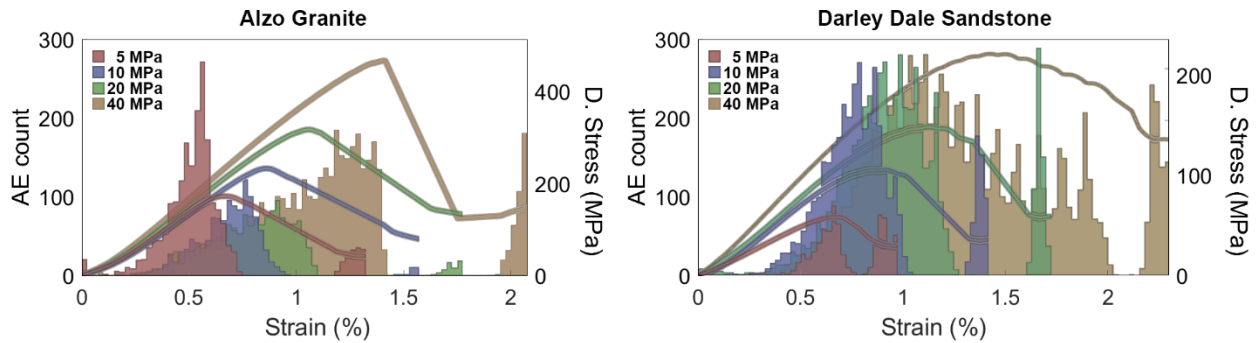
195 Figure 2: Slip vectors obtained from mechanism focal planes are first smoothed and interpolated onto a 3D grid. The  
 196 along strike component is set to zero and the divergence of this vector field is calculated to generate a 2D map.

197 For each mechanism category, a probability density function (PDF) is calculated for the time  
 198 of occurrence of individual AE as a function of strain. Low-amplitude data are defined as AE  
 199 with amplitudes in the bottom 5% of the total amplitude range for each mechanism of an  
 200 experiment. All three PDFs are then summed together, and a percentage contribution calculated.  
 201 This approach was selected instead of histogram bins as it generates a smoother distribution and  
 202 better highlights trends in the data. To ensure results are statistically relevant, the percentage  
 203 trend is sampled once every 10 events for a particular experiment and then smoothed in a moving  
 204 window of 0.04% strain. Results are split into three characteristic deformation stages that  
 205 correlate with periods of: 1) Fracture Nucleation and Fault Growth (0 - 70% UCS), 2) Crack  
 206 Coalescence (70 - 95% UCS), 3) Dynamic Failure of the sample (>95% UCS).

### 207 **3 RESULTS**

208 Mechanical Data highlight a progressive increase of peak strength with confining pressure  
 209 that is observed for both lithologies (**Figure 3**). For confining pressures of 5, 10, 20, and 40  
 210 MPa, dynamic failure of Alzo Granite occurs at peak stresses of 175 MPa, 240 MPa, 325 MPa  
 211 and 475 MPa respectively (**Figure 3**, left). Strain values at failure are 0.71%, 0.9%, 1.1% and

212 1.45% respectively. In each of the four experiments, an increase in AE is observed after a strain  
 213 of approximately 0.2%. For samples deformed at 5 and 10MPa, an approximate exponential  
 214 trend is seen in the counts of located AE after this point; however, for samples deformed at  
 215 higher confining pressure (20 and 40 MPa), the increase in AE count is more linear, increasing to  
 216 100 and 200 counts respectively at peak stress. In all experiments the maximum AE output is  
 217 seen to occur 0.1-0.2% before failure, signifying a high number of microcracks during the yield  
 218 stage of deformation, consistent with the timing of maximum AE observed in earlier work  
 219 (Benson et al., 2019).



220  
 221 Figure 3: Stress-Strain curves (line) and counts of located Acoustic Emission (AE, histogram) for Alzo Granite  
 222 (left) and Darley Dale Sandstone (right) as samples are deformed.

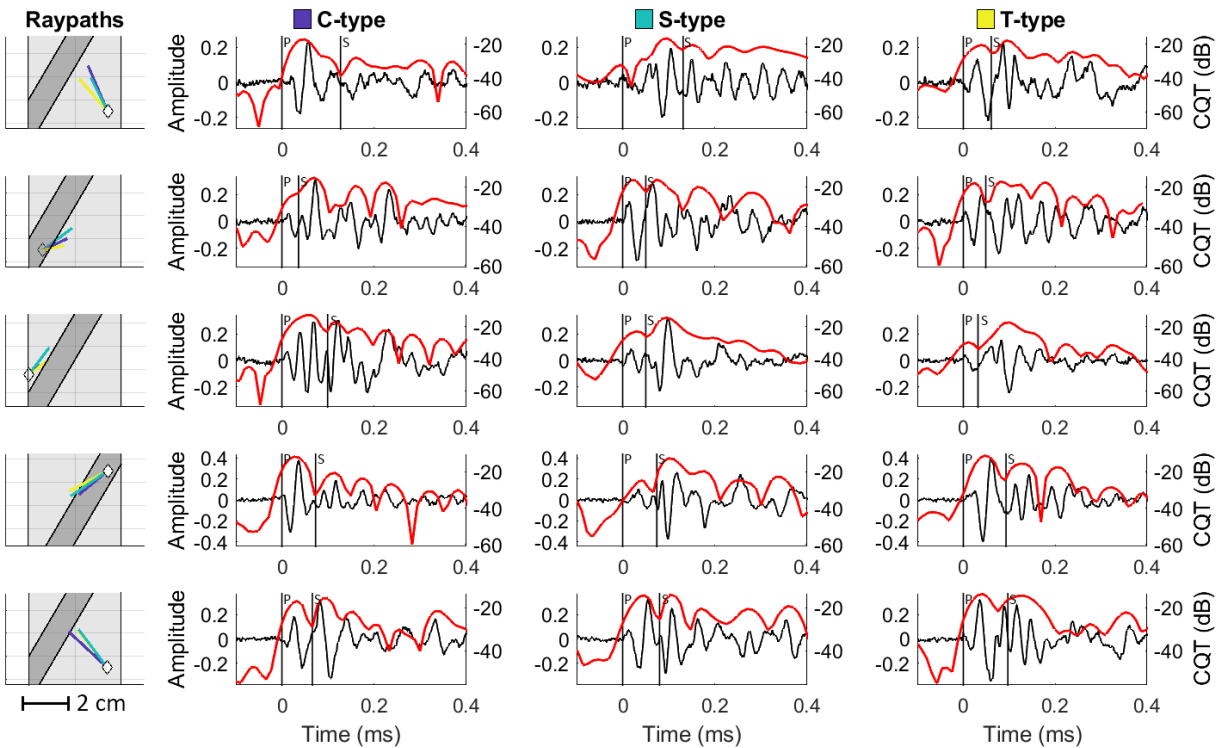
223 For Darley Dale Sandstone, dynamic failure of the sandstone samples occurs at peak stresses  
 224 of 60 MPa, 110 MPa, 150 MPa and 220 MPa for confining pressures of 5, 10, 20, and 40 MPa  
 225 respectively (**Figure 3**, right). The corresponding strain values at failure are 0.75%, 0.9%, 1.2%  
 226 and 1.3%. Unlike deformation in the Alzo Granite, failure of these samples is considerably more  
 227 gradual with a less pronounced stress drop. As confining pressure increases, a longer period of  
 228 strain softening (a slow decrease in differential stress as strain increases) is evident. In addition,  
 229 the AE count rate always increases with increasing confining pressure from strains of  
 230 approximately 0.5%. However, both the peak in AE count rate and the post-peak character show

231 some changes with increasing confining pressure. The AE peak occurs close to the peak stress at  
232 lower confining pressure while it shifts to earlier times in the strain curve at higher confining  
233 pressures. In addition, the post-peak behaviour is the same for stress and AE. Both show a quasi-  
234 ductile process, consistent with the smooth stress drop observed. A final burst of AE data after  
235 0.9, 1.2, 1.6 and 2.1% accompanies the final frictional sliding on the generated shear plane in  
236 each case, as also seen in the Alzo granite AE data.

### 237 **3.1 WAVEFORM CHARACTERISATION**

238 To aid in characterisation, S-wave onsets are automatically picked following a time-  
239 frequency transformation of the signal (Constant-Q Transform, CQT). The CQT is a technique  
240 that transforms a time-domain signal into the time-frequency domain with non-stationary Gabor  
241 frames, such that the centre frequencies of the frequency bins are logarithmically spaced, and  
242 their Q-factors are all equal. It is essentially a wavelet transform but with a higher potential  
243 resolution compared to conventional techniques (12-96 bins per octave). The Q-factor of bin  $k$  is  
244 defined as  $Q_k = \frac{f_k}{\Delta f_k} = \frac{N_k f_k}{\Delta \omega f_s}$ , where  $f_k$ ,  $\Delta f_k$  and  $\Delta \omega f_s$  denote the centre frequency, the -3 dB  
245 bandwidth of the frequency response and the -3 dB bandwidth of the mainlobe of the spectrum of  
246 the window function, respectively (Schörkhuber and Klapuri, 2010). The window length  $N_k$  is  
247 inversely proportional to  $f_k$  in order to have the same Q-factor for each bin. After computing the  
248 highest octave Q-factors over the entire signal, the input is lowpass filtered and downsampled by  
249 a factor of 2 in order to repeat the calculation for the desired number of octaves. For a full  
250 overview of please refer to Schörkhuber and Klapuri (2010) as it is not necessary to be aware of  
251 all the implementation details within the scope of this study. The S-wave onset is then defined as  
252 a local minimum in the CQT of the waveform bandpass filtered between 300 and 600 KHz,  
253 occurring shortly after the first pulse of the P-wave.

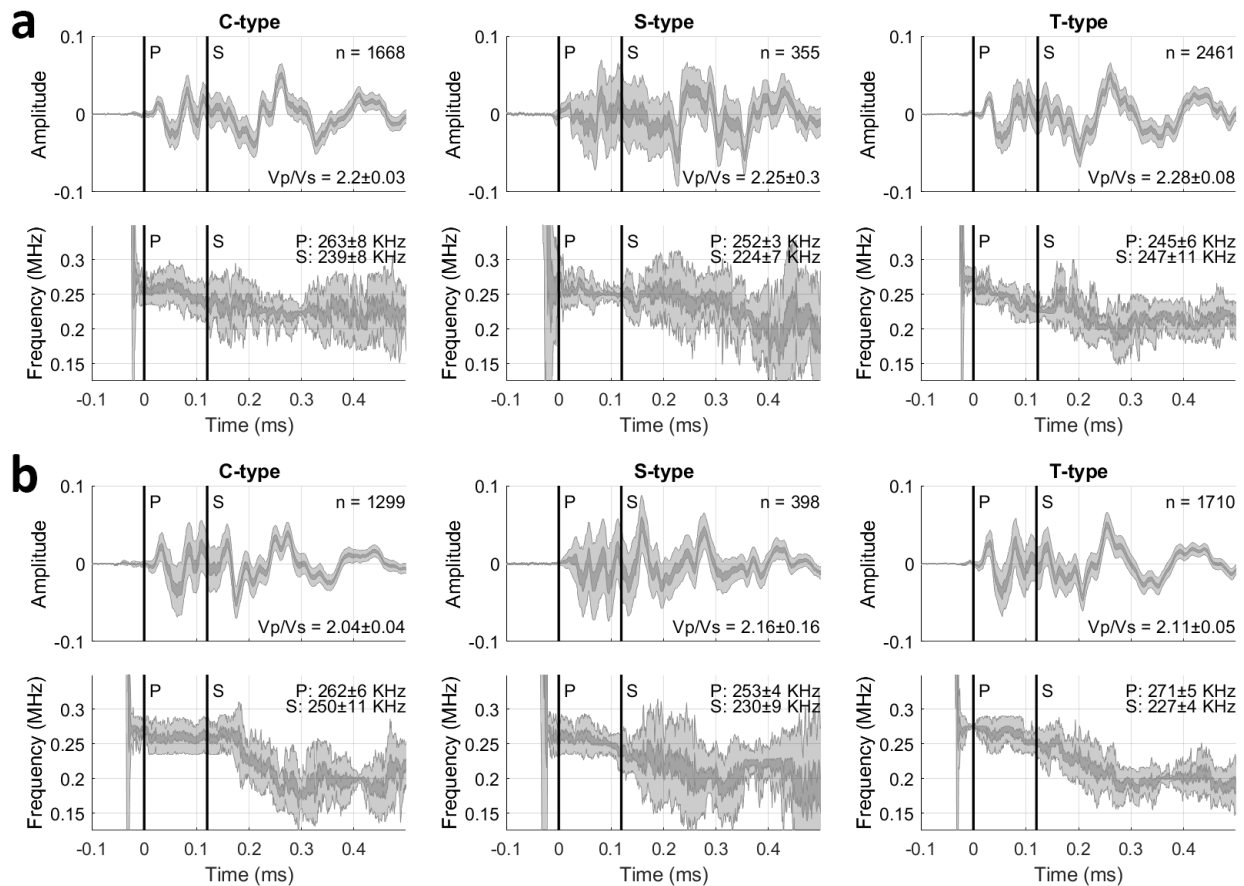
254 In order to determine what features may be related to the source, only the first arriving  
 255 waveform for AE is considered in this analysis (**Figure 4**). These typically only travel 1-2 cm  
 256 before reaching any receiver. Waveforms are further selected for AE with similar amplitudes and  
 257 that occur within 12.5 mm of each other, approximately one wavelength. To minimise the  
 258 influence of time-varying structure whilst ensuring a representative from each mechanism type  
 259 (columns), events are also windowed to occur within 4 minutes of each other (rows). Waveforms  
 260 are presented with corresponding raypaths (first column) and the CQT (red line) which has been  
 261 used to define the S-wave onset. Vertical black lines indicate estimated P- and S-wave arrivals.



262

263 Figure 4: Example waveforms for each mechanism type (columns) that occur close in space and time to each other  
 264 (rows). The first column indicates raypaths of events to a receiver (diamond). A dark grey region is used to indicate  
 265 the main fault zone. Waveforms are presented with their corresponding Constant-Q Transform that is used to  
 266 estimate the S-wave onset.

267 Path-dependent effects dominate the waveform from the early onset, and it is difficult to  
 268 discriminate the properties of individual source types. High amplitude reflections from near-  
 269 source scattering are observed to overlap estimated S-wave arrivals (e.g. bottom row, **Figure 4**).  
 270 Additional reflections can also be observed arriving approximately 0.2 ms after the P-wave onset  
 271 and may relate to the sample boundaries (e.g. middle row, **Figure 4**). However, these  
 272 observations would require advanced modelling of the medium to verify and should be taken  
 273 with caution.



274  
 275 Figure 5: Average waveform and dominant frequency content for n number of waveforms. Vertical bars indicate  
 276 average P- and S-wave onsets. a) Alzo Granite. b) Darley Dale Sandstone.

277 Nonetheless, the CQT does show potential for highlighting individual phase arrivals. The  
 278 average waveforms for AG (**Figure 5a**) and DDS (**Figure 5b**) are presented with the

279 bootstrapped modal frequency content (Hilbert transform). The grey regions indicate the  
280 standard deviation (1 and 1/5) of the bootstrapped timeseries' for  $n$  number of waveforms.  
281 Vertical black bars indicate the average P- and S-wave arrival times. Here, the onset of the S-  
282 wave is characterised by an approximate 30 KHz reduction in dominant frequency content that  
283 occurs regardless of mechanism type. However, modifying confining pressure from 5 to 40 MPa  
284 resulted in an approximately 80 KHz increase in the average frequency content of AE in DDS. A  
285 similar trend was observed in AG, but strong scattering of the waveform resulted in significant  
286 uncertainty in the dominant frequency characteristics (compare bottom rows for **Figures 5a** and  
287 **5b**).

288 Average  $V_p/V_s$  ratios are on average higher than has been previously reported (1.41 – 2.02  
289 for sandstones, e.g. Zhang & Bentley, 2003), at approximately 2.1 for DDS and 2.25 for AG. At  
290 the short hypocentral distances investigated here, dominant frequencies are well within the near-  
291 field scattering regime, where the splitting intensity of the S-wave is predicted to be very low  
292 (Favier et al., 2004). As a high  $V_p/V_s$  ratio is further predicted in the absence of S-wave splitting  
293 (Wang et al., 2012), the values presented here may represent differences in the fracturing process  
294 between the two rock types. However, due to the overlapping error ranges, it is difficult to  
295 identify clear differences between the three mechanisms. Although random subsampling of the  
296 data does suggest a more scattered transition between P- and S-waves for S-type events that  
297 would result in the higher  $V_p/V_s$  ranges observed, where an earlier dominance in low frequency  
298 energy can occur in the P-wave for S-type fracturing. This is distinct from C- and T-type events  
299 where higher frequency energy is instead preserved into the early S-wave.

300 **3.2 SOURCE ORIENTATIONS AND LOCATION**

301 AG and DDS demonstrate broadly similar trends in the relative distribution of fracturing  
 302 mechanisms. Clear dominance of T-type fracturing is present at all confining pressures with  
 303 typical counts two to three times larger than C-type fracturing. S-type fracturing occurs in very  
 304 low numbers, although counts are larger in the sandstone than in the granite. Average  
 305 orientations of fracture mechanisms are detailed in **Figure 6** and compared with confining  
 306 pressure. Circular points indicate the average of each of the mechanism types at the different  
 307 confining pressures. Error bars are calculated as the standard deviation above and below the  
 308 mean value and represent the spread of the data.

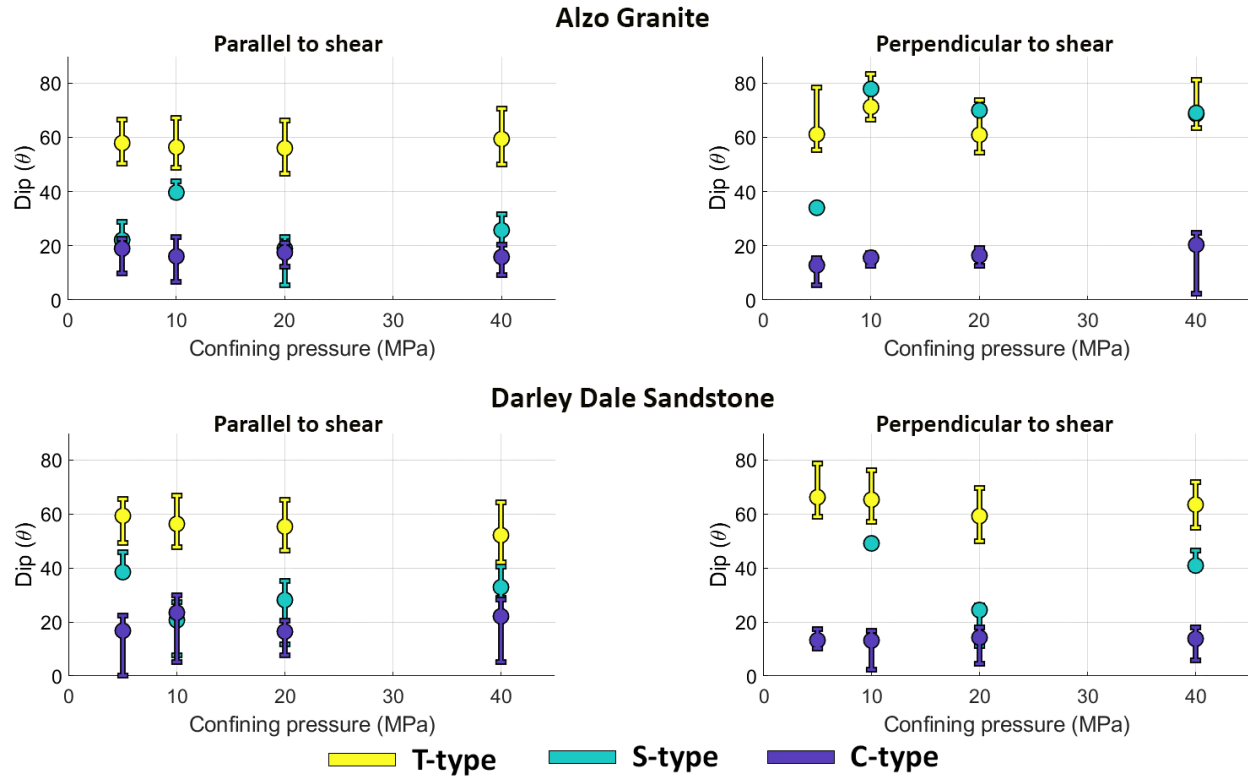
309 Table 2: Counts of solved mechanisms of C-type, S-type and T-type fracturing. Data are separated into groups that  
 310 dip parallel or perpendicular to the principle shear direction. A dominance of T-type fracturing is observed for all  
 311 samples, followed by C-type. Counts of S-type events are remarkably low for both rock types. Highlighted  
 312 conditions and values have been chosen for analysis in Figure 7-Figure 11.

Rock Type	Pressure (MPa)	Parallel to Shear			Perpendicular to Shear		
		T-type	S-type	C-type	T-type	S-type	C-type
<b>Alzo Granite</b>	<b>5</b>	<b>1103</b>	<b>64</b>	<b>325</b>	<b>489</b>	<b>11</b>	<b>252</b>
	10	705	45	109	390	8	132
	20	847	84	387	451	17	245
	40	2353	283	813	1113	12	293
<b>Darley Dale Sandstone</b>	5	440	22	198	151	0	58
	10	1465	161	822	1202	11	653
	<b>20</b>	<b>2493</b>	<b>137</b>	<b>822</b>	<b>1671</b>	<b>112</b>	<b>620</b>

313

---

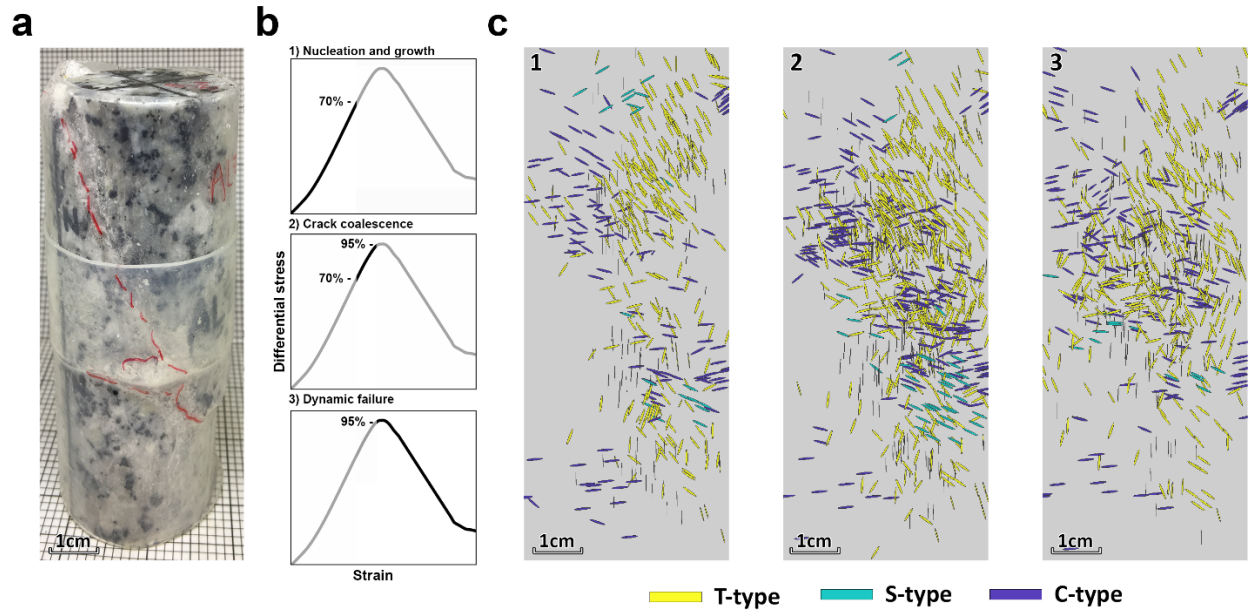
314 For both rock types, T-type events are orientated generally perpendicular (dips higher than  
315  $60^\circ$ ) to the direction of principal stress, whilst C-type events show the opposite trend with sub-  
316 horizontal fracturing (dips less than  $20^\circ$ ). S-type events are found across a range of dips between  
317  $20^\circ$  and  $60^\circ$ . Although dip trends for all mechanisms are generally consistent as confining  
318 pressure increases, there is a notable rotation of shear-parallel T- and S-type in DDS that is  
319 consistent with previous observations of strain localisation (e.g. Mair et al., 2002). At low  
320 confinements, deformation principally occurs in bands parallel to the main direction of  
321 compression. As stress increases, these bands develop a shear-component causing the angle  
322 between the most compressive direction and the band to increase (Bésuelle, 2001). However, this  
323 trend is not present in AG, where instead shear parallel T- and S-type follow opposed trends with  
324 shear perpendicular C-type events steepening as confining pressure increases.



325

326 Figure 6: Average mechanism orientations are plotted against confining pressure for events dipping parallel or  
 327 perpendicular to the sample failure plane. Error bars are defined as the standard error and represent the range of data  
 328 from which the average is calculated

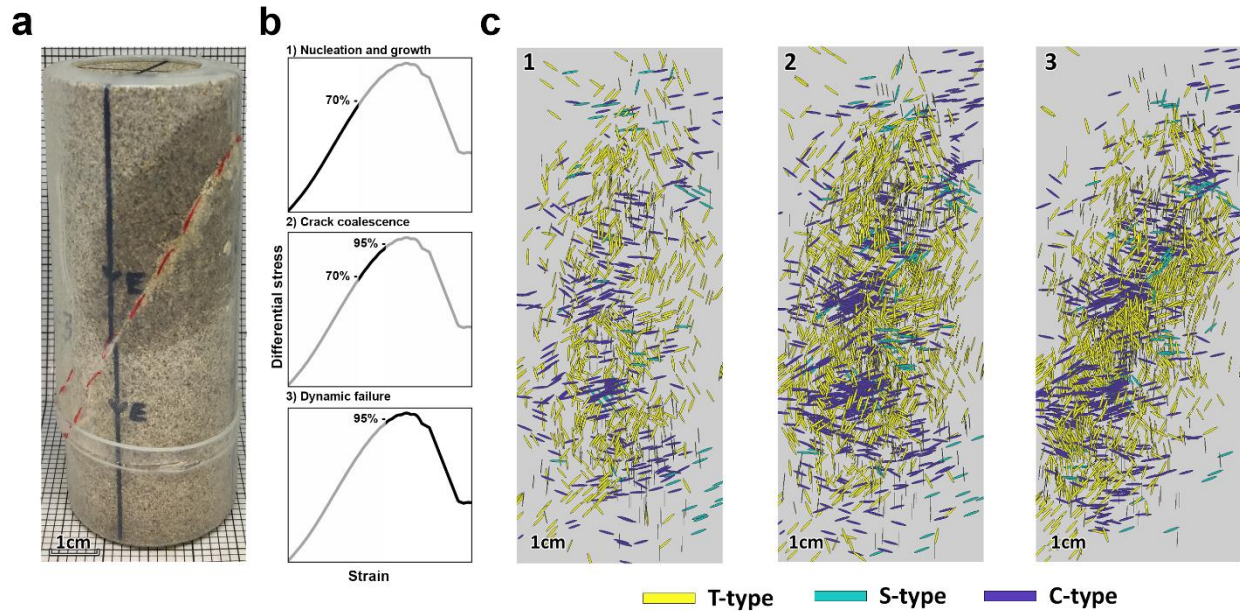
329 To analyse the time and spatial evolution of the source mechanisms with relation to the  
 330 evolving mechanical steps, the following key periods are selected: 1) Fracture Nucleation and  
 331 growth, 2) Crack Coalescence and 3) Dynamic Failure. Mechanism orientations are first  
 332 presented, then divergence maps are shown to highlight a simplified fracture pattern, and finally  
 333 percentage mechanisms trends are shown for AG data collected at 5 MPa confining pressure and  
 334 DDS data at 20 MPa. These were selected as they highlighted the most representative patterns  
 335 observed in the formation and evolution of the fault zone (supplementary material for detail of  
 336 experimental conditions).



337

338 Figure 7: a) Post-deformation photo of Alzo Granite deformed at 5 MPa. b) Simple stress vs. strain plots indicating  
 339 time periods. c) Spatial distribution of solved focal mechanisms in windows of 1) Fracture Nucleation and Growth,  
 340 2) Crack Coalescence and 3) Dynamic Failure. Grey region indicates sample dimensions.

341 Post-deformation imaging in AG at 5 MPa and DDS at 20 MPa (hereafter referred to as  
 342 AG\_5 and DDS\_20) reveals relatively simple surface expressions of newly formed fracture  
 343 structures (dashed red line - **Figure 7a** and **Figure 8a**, respectively). Sample AG\_5 (**Figure 7c**)  
 344 demonstrates axial splitting in the form of T-type during the whole experiment: characteristically  
 345 steeply-dipping ( $>60^\circ$ ) events with no clear preference in the dip direction or positioning (i.e. on-  
 346 or off-fault, Aben et al., 2019). Two potential faults extending from the left corners are  
 347 highlighted by the distribution of C-type fracturing during period 1. An increase in fault-parallel  
 348 S-type events during period 2 identifies the eventual failure direction with C-type localising  
 349 along the failure plane. Following dynamic failure (period 3), fracturing events remain strongly  
 350 diffuse throughout the sample.



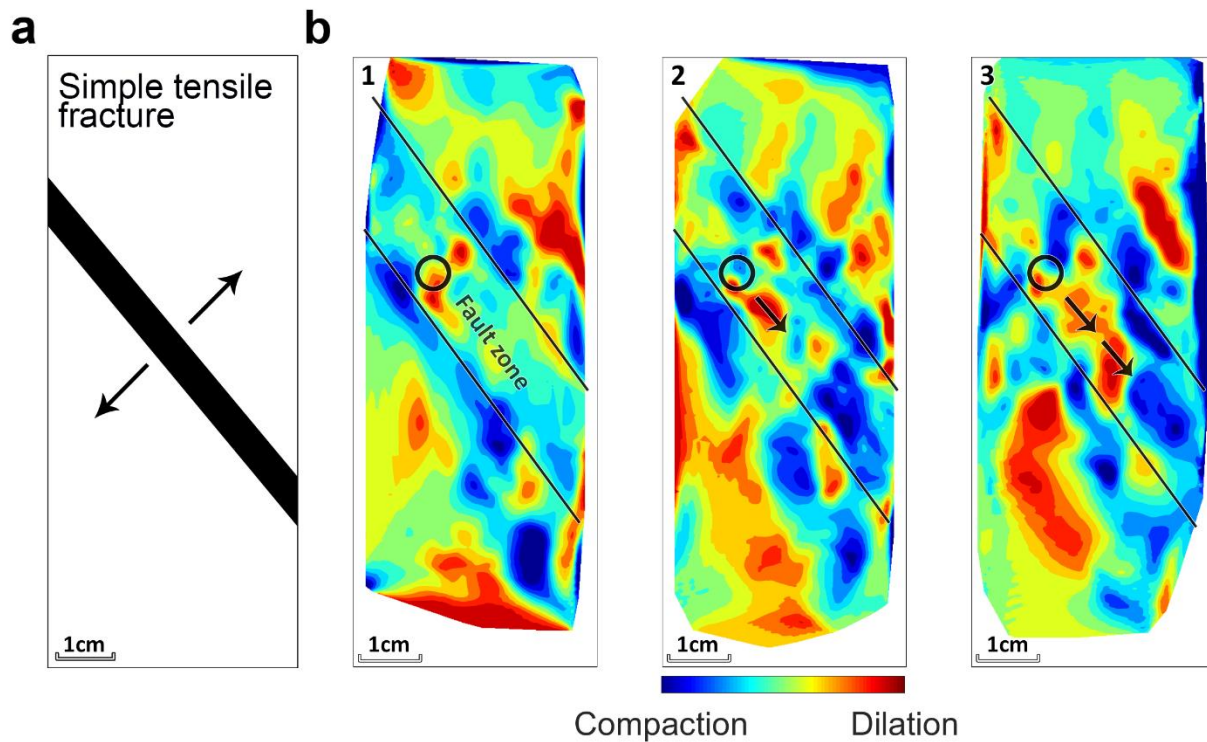
351

352 Figure 8: a) Post-deformation photo of Darley Dale Sandstone deformed at 20 MPa. b) Simple stress vs. strain plots  
 353 indicating time periods. c) Spatial distribution of solved focal mechanisms in windows of 1) Fracture Nucleation and  
 354 Growth, 2) Crack Coalescence and 3) Dynamic Failure. Grey region indicates sample dimensions.

355 Sample DDS\_20 reveals an overall trend for strain localisation, with more events  
 356 attributed to the eventual failure plane as deformation progresses (**Figure 8c**). The event  
 357 locations are diffused throughout the sample during the early stages of deformation. As strain  
 358 increases, a leftward-dipping region of sub-horizontal C-type events precedes a bulk rotation of  
 359 source locations (period 1). Like AG\_5, two potential faults extending from the right-hand  
 360 corners are visible. During crack coalescence (period 2) T-type events localise to both an upper  
 361 cluster and a central 45°-dipping lineation. Following failure (period 3), C-type locations are  
 362 consistent with the post-test imagery of the final fault (e.g. Benson et al., 2010; Lockner et al.,  
 363 1992), with T-type fracturing occurring along a 45° band. S-type fracturing remains diffuse in the  
 364 sample throughout the whole experiment. Although events dip in the same direction as the  
 365 developing fault zone, source locations do not highlight how these events relate to the macro-  
 366 structure.

367 **3.3 DILATANCY VS. COMPACTION**

368 In order to further investigate the competing mechanisms, divergence maps of mechanism  
369 slip vectors were derived (**Figure 9** and **Figure 10**). An important distinction of these maps is  
370 that regions of compaction and dilatancy do not necessarily correlate with the distribution of C-  
371 and T-type mechanisms previously discussed. Similar to results obtained via 3D X-Ray  
372 Tomography (Renard et al., 2019), they represent the general stress field of the samples as they  
373 undergo deformation and reveal how dislocations caused by the different fracture mechanisms  
374 interact with each other over longer distances (Zang and Stephansson, 2010). Due to the  
375 smoothing imposed by the interpolation (**Figure 2**) anomalies have a minimum dimension of ~1  
376 cm.

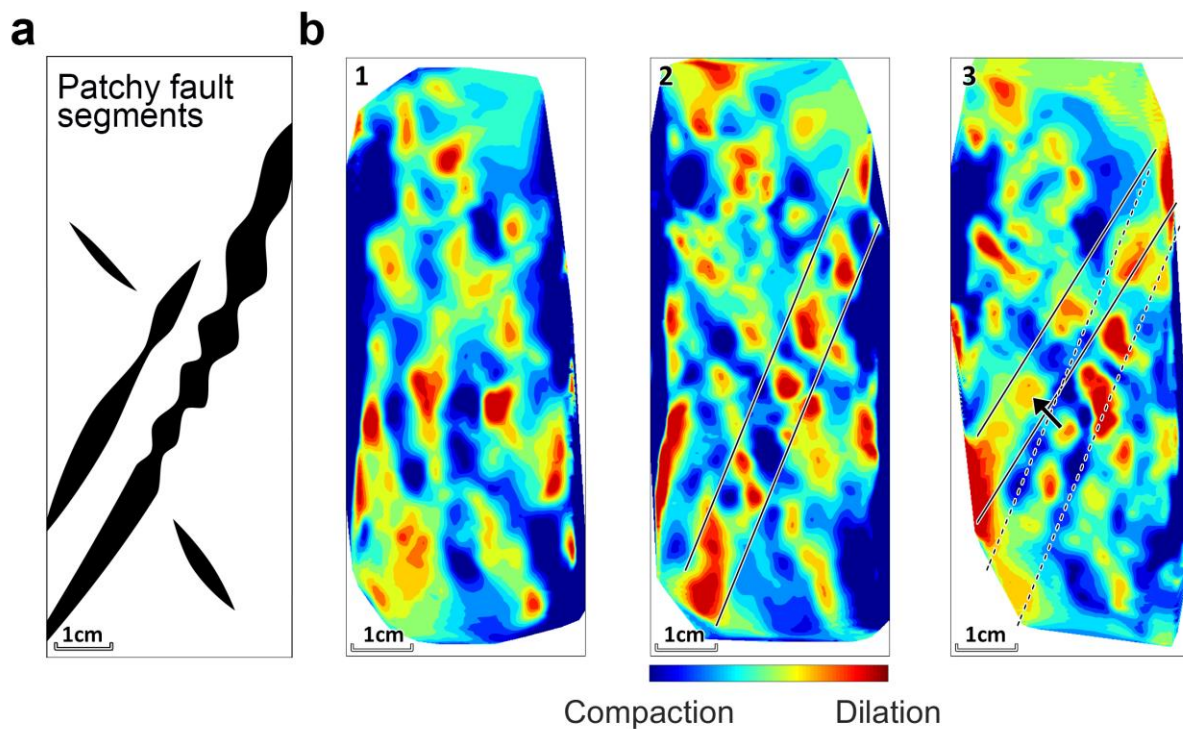


377

378 Figure 9: a) Simplified fracture pattern in Alzo Granite deformed at 5 MPa. b) Divergence maps of mechanism slip  
379 vectors. Red regions indicate dilatational regions where vector directions are diverging. Blue indicates compactant  
380 regions where vector directions are converging. Data are windowed into periods of 1) Fracture Nucleation and

381 Growth, 2) Crack Coalescence and 3) Dynamic Failure. Circles indicate a fracture nucleation point, whilst arrows  
382 highlight the direction of fracture propagation.

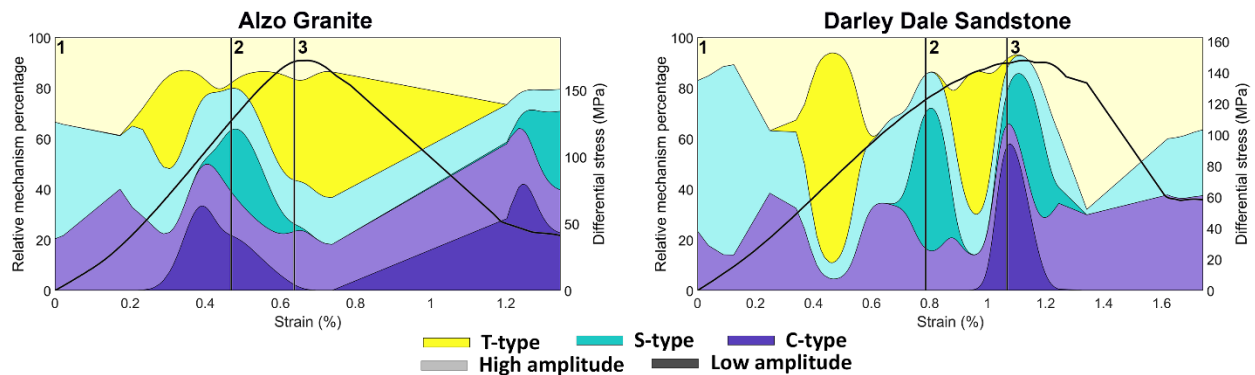
383 A central rightward-dipping region of dilatancy characterises the fault zone in AG\_5  
384 (Figure 9). The edges of the fault are delineated by strong compaction anomalies from the start  
385 of the experiment. This is either caused by expansion of the fault core interacting with broad  
386 dilation anomalies to the top right and bottom left of the sample, or due to real compaction along  
387 the edges of the fault zone. A strong dilation anomaly (Figure 9b, circled) in top left portion of  
388 the fault zone (period 1) is observed to compact and then propagate down and along the fault  
389 zone during periods 2 and 3.



390

391 Figure 10: a) Simplified fracture pattern for Darley Dale Sandstone deformed at 20 MPa. b) Divergence maps of  
392 mechanism slip vectors. Red regions indicate dilatational regions where vector directions are diverging. Blue  
393 indicates compactant regions where vector directions are converging. Data are windowed into periods of 1) Fracture  
394 Nucleation and Growth, 2) Crack Coalescence and 3) Dynamic Failure. Rectangular regions and arrow highlight a  
395 switch in the dilating region during period 3.

396 Unlike AG\_5, which is characterised by a single fault throughout the test, DDS\_20  
 397 demonstrates multiple, unrelated sources of dilatant fracturing (**Figure 10b**). Compaction  
 398 follows a similarly broadly distributed trend delineating regions of sub-vertical dilation that may  
 399 be analogous to the formation of axial splitting (period 1). As strain increases into period 2,  
 400 anomalies are observed to connect into linear structures. Dilation anomalies not associated to this  
 401 “connection” of structure also weaken, with some areas becoming dominated by compaction.  
 402 However, these trends should be considered with caution as we do not consider the size of  
 403 individual sources. A 60° lineation of dilatancy dominates the divergence field at this time,  
 404 however, it is not entirely associated to observed failure structure in the post-test imagery  
 405 (**Figure 8a**). Instead, dilation switches to a higher fault during dynamic failure of the sample  
 406 with anomalies mainly extending from the top right to the bottom left (period 3).



407 Figure 11: Mechanism percentage trends for Alzo Granite deformed at 5MPa (left) and Darley Dale Sandstone  
 408 deformed at 20 MPa (right). The changing dominance of T-type (yellow), S-type (green) and C-type (blue) events  
 409 separated by amplitude (lighter for high, darker for low) is observed as strain increases. Data are windowed into  
 410 periods of 1) Fracture Nucleation and Growth, 2) Crack Coalescence and 3) Dynamic Failure.  
 411

412 **Figure 9** and **10** reveal a relationship between regions of compaction and patchy dilatancy;  
 413 however, the spatial mapping is insufficient to understand if they are antagonistic or in  
 414 accordance. Percentage trends of the probability of fracturing mechanisms (**Figure 11**) highlight  
 415 the variations in dominance of C-, S- and T-type events as deformation progresses. The pattern

416 of low-amplitude events (darker colours) reveals an underlying periodicity to the development of  
417 fracture structure where mechanisms transition in sequences. It is important to note that these are  
418 not a percentage of event counts, rather they are the percentage of the probability (or likelihood)  
419 of a specific mechanism occurring.

420 During period 1, high-amplitude C- and T-type fracturing are in accordance with each other  
421 for both samples. However, S-type events are more frequent in DDS\_20 during this time than at  
422 later stages. At 0.3% and 0.45% strain (AG and DDS respectively), there is a burst of low-  
423 amplitude T-type events that is related to the early axial splitting observed in the spatial  
424 mapping. This occurs before a periodic cycle of fracture development (period 2) during the  
425 elastic phase of deformation, where C-type events (0.4% and 0.65%) transition into S-type  
426 fractures (0.5% and 0.8%). The fractures peak at the start of crack coalescence before changing  
427 to T-type (0.6% and 0.95%). The antagonistic cycle between high-amplitude T- and C-type  
428 events (lighter colours, **Figure 11**) occurs once in AG\_5 (strains of 0.3% - 0.65%) and twice in  
429 DDS\_20 (period 2 - 0.6% - 0.95%; period 3 - 1% - 1.3%). Unlike their high-amplitude events  
430 counterparts, there is no apparent antagonistic cycle between low-amplitude T- and C-type  
431 (darker colour, **Figure 11**), suggesting that this only develops later during deformation. In both  
432 samples, dynamic failure is dominated by T-type fracturing with only a minor contribution of S-  
433 type.

#### 434 **4 DISCUSSION**

435 This study has analysed fault zone development in Alzo Granite and Darley Dale Sandstone  
436 through characterisation of individual AE source mechanisms using a modified first-motion  
437 polarity method. Data are broken up into characteristic periods of 1) Fracture Nucleation and  
438 Growth, 2) Crack Coalescence and 3) Dynamic Failure. This method differs from the average

439 polarity approach (e.g. Stanchits et al., 2006) by projecting measurements onto idealised focal  
440 spheres. The advantage of this method is that it better accounts for the 3D geometry of the source  
441 rather than assuming a dominance of either polarity to categorise events. A limitation is that  
442 results can be biased by the models used to fit the data. For instance, a looser definition of what  
443 marks a shear event would likely increase the number of events characterised here as S-type.  
444 Furthermore, tensile-shear (Liu et al., 2019) or compaction-shear (Bésuelle, 2001) events are  
445 likely to be marked as T- or C-type, respectively. Due to computational limitations it is  
446 unfeasible to address the full spectrum of fracturing types, nonetheless the results of this study  
447 demonstrate systematic variations in fracture development that can be attributed to the pre-  
448 existing conditions of the sample, i.e., cohesive or granular, and the confining pressure applied  
449 during deformation.

450 The distribution of C-type fractures in **Figure 7c** shows that the failure plane nucleates at the  
451 edges of the sample (Benson et al., 2007) or is at least heavily influenced by them, with two  
452 potential faults visible in AG\_5 during period 1. This observation implies that C-type events are  
453 an important precursor to crack coalescence. This is confirmed in DDS\_20, where C-type  
454 fracturing dominates the failure plane throughout deformation (**Figure 8c**). Interestingly, there  
455 are isolated C-type events that are not associated to any prior fracturing, for instance in the top  
456 left of AG\_5 in period 1 (**Figure 7c**). Within the sandstone this can be easily explained through  
457 mechanisms of pore collapse (Zhu et al., 2010), but this is unlikely in the granite, especially  
458 during the early stages of deformation. More likely, they represent a hybrid mode of compaction-  
459 tensile fracturing (CT-type). These low angle events form as part of a continuous transition  
460 between extension (tensile) and shear fracturing, and are thought to occur under mixed tensile  
461 and compressive stress conditions (Ramsey and Chester, 2004). In the Mount Desert Island

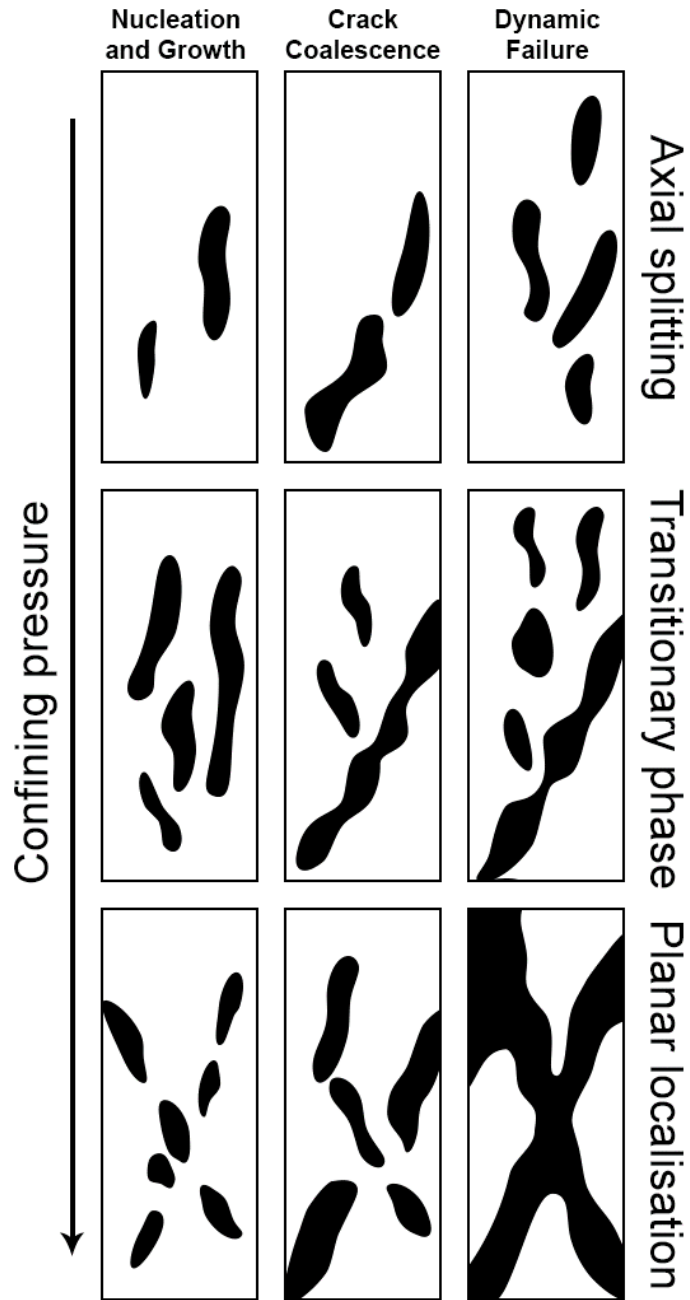
462 Granite, stepped fracture geometry, consistent with fracture formation via linkage of en-echelon  
463 arrays, were identified as hybrid (CT) fractures (Engelder, 1999, 1989). The results reported in  
464 this study suggest that CT-type events form during the earliest stages of fault zone formation (i.e.  
465 period 1) before any larger scale structure dominates the stress field.

466 A steepening of S-type and a shallowing of T-type events with increasing confining pressure  
467 in **Figure 6** represents a switch from axial splitting to fault plane localisation in DDS (Mair et  
468 al., 2002; Passelègue et al., 2016). AG demonstrates the opposite trend where S-type events  
469 become shallower and T-type steepen. Furthermore, there is a steepening of C-type events in the  
470 perpendicular direction. It is likely that these rotations occur as a result of the same transitional  
471 switch present in DDS. However in samples of granite, X-ray tomography reveals that crack  
472 growth can be hampered by minerals and grain boundaries leading to closure near to the fracture  
473 tip (McBeck et al., 2019). In the case of AG, the presence of large feldspar grains can inhibit the  
474 propagation of S-type events (Yu et al., 2018; Zhao et al., 2019). Instead, these events will occur  
475 as C-type with fracturing developing perpendicular to the direction of shear. This shear inhibition  
476 will further reflect on shear-parallel T-type events, raising the average dip as more events  
477 become localised along the failure plane at higher confining pressures. This is consistent with the  
478 observation that the strength of a material dictates how and where a fracture will propagate  
479 (McBeck et al., 2017).

480 The presence of single or multi- periodic fracture growth in AG\_5 and DDS\_20,  
481 respectively (**Figure 11**), is likely related to the initial patchiness of dilatant regions. These  
482 cycles begin as a dominance of C- and S-type fracturing before transitioning to bursts of T-type  
483 events. This double-yielding behaviour has been previously seen in triaxially compressed porous  
484 limestone (Huang et al., 2019). The authors observed cataclastic pore collapse, driven by shear

485 enhanced compaction, preceding the development of widespread bifurcation. In AG\_5, the end  
486 of this sequence results in dynamic failure of the sample, whilst in DDS\_20 the cycle occurs  
487 twice. When an earthquake ruptures, it is likely to trigger an event on an adjacent fault due to  
488 perturbations of the local stress field (Wesnousky, 2006). As a result, clustered fractures are  
489 more likely to propagate than dispersed structure (McBeck et al., 2019). The mechanism  
490 divergence maps for AG\_5 suggest that failure occurred due to the rupture of a single region of  
491 dilatancy in period 2 (**Figure 9b**). However, the dispersed structure of DDS\_20 required an  
492 initial growth cycle to first align fracture segments before a second cycle resulted in sample  
493 failure (**Figure 10b** and **Figure 11**, right).

494 Laboratory and numerical studies highlight creep patches or deformable bodies that occur  
495 prior to fault coalescence (e.g. Aldam et al., 2017; Kaneko and Lapusta, 2008). This has been  
496 interpreted to be analogous to foreshock sequences prior to a main shock earthquake (Kato et al.,  
497 2012; Latour et al., 2013). A meta-study on the occurrence of foreshocks debated their existence  
498 as either the result of tectonic loading or that they may reflect a triggering/excitation process  
499 (Mignan, 2014). The author concluded that this could only be resolved through large datasets  
500 that included significant amounts of microseismicity due to biases imposed by data selection. In  
501 **Figure 11**, the occurrence of low amplitude C- and S-type events prior to bursts of T-type  
502 activity leading to planar localisation well represents the premonitory phase, or foreshock, before  
503 a critical damage threshold would allow the coalescence into a larger scale deformation structure.



504

505 Figure 12: Simplified brittle failure patterns. Dilatant regions (black) highlight the changing distribution of  
 506 deformation structure as confining pressure increases for the different deformation stages. A transitional phase  
 507 between axial splitting is identified where zones of deformation form into planar structure during crack coalescence.

508 In samples of Westerly Granite, Passelègue et al. (2016) identified transitional phases  
 509 between axial splitting at low pressures to shear localisation at higher confinement as the sample

510 fails. The mechanism divergence maps of all the analysed pressures support this observation (see  
511 supplementary) and are summarised in **Figure 12** as simplified brittle failure patterns. At low  
512 pressures the fracture energy of a fault is similar to that of minerals (Passelegue et al., 2016),  
513 where small asperities throughout the sample can accommodate strain resulting in a diffuse  
514 pattern of dilatancy. Under higher stress conditions the energy required to propagate a fracture is  
515 much larger, so only flaws that are preferentially aligned to the internal stress field will rupture.  
516 The samples analysed here were undamaged at the start of deformation, therefore the alignment  
517 of easy-to-rupture flaws will be unlikely. At transitional pressures, it is only when the  
518 concentration of dilatant regions reaches a threshold that axial splitting switches to localisation  
519 (e.g. period 2 in DDS\_20 - **Figure 10b**). During period 1 and once confining pressures are  
520 sufficiently high, long-range elastic interactions between flaws in the sample allow for failure  
521 plane structures to localise earlier (Kandula et al., 2019).

## 522 **5 CONCLUSIONS**

523 The aim of this study was to identify patterns in the fracture development process by  
524 mapping rupture source mechanisms (tensile, shear, collapse) derived from microseismic  
525 signatures (AE) recorded during conventional triaxial deformation experiments. Two lithologies,  
526 representing end members in terms of rock physical properties (e.g. fabric, porosity, grain size,  
527 cementation), were used: Alzo Granite (AG), Italy and Darley Dale Sandstone (DDS), United  
528 Kingdom. Unlike the commonly used average polarity method (e.g. Stanchits et al., 2006) the  
529 approach reported here uses the source radiation pattern (Kwiatek and Ben-Zion, 2013) to  
530 categorise events and obtain source orientations of mixed-mode type mechanisms.

531 AE data from conventional triaxial compression tests of Alzo Granite and Darley Dale  
532 Sandstone at confining pressures of 5-40MPa were investigated to identify evolving damage

533 mechanisms process by mapping rupture source mechanisms using a least-squares minimisation  
534 of the 3D focal sphere to classify fracturing mechanisms as tensile, shear or compaction. Results  
535 highlight a complex interplay between compactant (C-type) and dilatant (T-type) fracturing  
536 processes leading to the formation of the fault zone that is consistent in both lithologies. C-type  
537 events are the earliest precursor, identifying initial fault planes during crack nucleation. Low  
538 amplitude T-type events mark new cracks opening and the onset of fracture growth. This period  
539 of deformation induced fracture growth is characterised by periodic cycles of coalescence,  
540 transitioning from C- to shear (S-type) and then back to T-type events. At the end of each  
541 sequence, macroscopic structure forms. For Alzo Granite, a single damage cycle is sufficient to  
542 develop the planar localisation leading to dynamic failure. Whilst in Darley Dale Sandstone it  
543 can take multiple cycles for coalescence to take place due to interacting mechanisms induced by  
544 multiple fracture nucleation sites.

545 The results of this study can have several implications for the interpretation of natural  
546 earthquakes precursors. The occurrence of C- and S-type events prior to bursts of T-type activity  
547 leading to planar localisation well represents the premonitory phase, or foreshock, before a  
548 critical damage threshold would allow the coalescence into a larger scale deformation structure.  
549 Results also provide new insights for developing new monitoring strategies for earthquake  
550 precursory detection. The identification of C- and S- type events could provide an early warning  
551 signature before premonitory slip occurs.

## 552 **6 DATA AND RESOURCES**

553 Acoustic Emission data are obtained at the Rock Mechanics Laboratory, University of  
554 Portsmouth. Due to the size of the datasets, Acoustic Emission are unavailable. Programming  
555 codes were developed in MATLAB® version 2018a and are available at  
556 <https://zenodo.org/record/4059413#.X3Rh4xfhPY>.

557 **7 ACKNOWLEDGEMENTS**

558 The authors thank Emily Butcher for sample preparation and Peter Ibemesi for assistance  
559 during the laboratory experiments. The authors greatly appreciate the efforts of one anonymous  
560 reviewer and Jessica McBeck in significantly improving the quality of this study.

561 **8 REFERENCES**

- 562 Aben, F.M., Brantut, N., Mitchell, T.M., David, E.C., 2019. Rupture Energetics in Crustal Rock  
563 From Laboratory-Scale Seismic Tomography. *Geophys. Res. Lett.* 46, 7337–7344.
- 564 Aldam, M., Weikamp, M., Spatschek, R., Brener, E.A., Bouchbinder, E., 2017. Critical  
565 Nucleation Length for Accelerating Frictional Slip. *Geophys. Res. Lett.* 44, 11,390-  
566 11,398. <https://doi.org/10.1002/2017GL074939>
- 567 Ashby, M.F., Hallam, S.D., 1986. The failure of brittle solids containing small cracks under  
568 compressive stress states. *Acta Metall.* 34, 497–510.
- 569 Baud, P., Meredith, P., 1997. Damage accumulation during triaxial creep of Darley Dale  
570 sandstone from pore volumetry and acoustic emission. *Int. J. Rock Mech. Min. Sci.*  
571 34, 24-e1.
- 572 Baud, P., Wong, T., Zhu, W., 2014. Effects of porosity and crack density on the compressive  
573 strength of rocks. *Int. J. Rock Mech. Min. Sci.* 67, 202–211.
- 574 Benson, P.M., Austria, D.C., Gehne, S., Butcher, E., Harnett, C.E., Fazio, M., Rowley, P.,  
575 Tomas, R., 2019. Laboratory simulations of fluid-induced seismicity, hydraulic fracture,  
576 and fluid flow. *Geomech. Energy Environ.* 100169.  
577 <https://doi.org/10.1016/j.gete.2019.100169>
- 578 Benson, P.M., Thompson, B.D., Meredith, P.G., Vinciguerra, S., Young, R.P., 2007. Imaging  
579 slow failure in triaxially deformed Etna basalt using 3D acoustic-emission location and  
580 X-ray computed tomography. *Geophys. Res. Lett.* 34.  
581 <https://doi.org/10.1029/2006gl028721>
- 582 Benson, P.M., Vinciguerra, S., Meredith, P.G., Young, R.P., 2010. Spatio-temporal evolution of  
583 volcano seismicity: A laboratory study. *Earth Planet. Sci. Lett.* 297, 315–323.
- 584 Bésuelle, P., 2001. Evolution of strain localisation with stress in a sandstone: Brittle and semi-  
585 brittle regimes. *Phys. Chem. Earth Part Solid Earth Geod.* 26, 101–106.  
586 [https://doi.org/10.1016/S1464-1895\(01\)00032-1](https://doi.org/10.1016/S1464-1895(01)00032-1)
- 587 Bésuelle, Pierre, 2001. Compacting and dilating shear bands in porous rock: Theoretical and  
588 experimental conditions. *J. Geophys. Res. Solid Earth* 106, 13435–13442.
- 589 Bugini, R., Pavese, A., Borroni, S., Folli, L., 2000. White granites used in Lombard architecture,  
590 in: *Proceedings of the 9th International Congress on Deterioration and Conservation of*  
591 *Stone.* Elsevier, pp. 41–48.
- 592 Cavallo, A., Bigioggero, B., Colombo, A., Tunesi, A., 2004. The Verbano Cusio Ossola  
593 province: a land of quarries in northern Italy (Piedmont). *Miner.* 73, 197.
- 594 Chen, H.K., Zhou, Y.T., Wang, Z., 2014. Study on Damage Characteristics of Unstable Rocks  
595 under Excitation Effect, in: *Applied Mechanics and Materials.* Trans Tech Publ, pp. 575–  
596 581.
- 597 Comanducci, L., Cobos, M., Antonacci, F., Sarti, A., 2020. Time Difference of Arrival  
598 Estimation from Frequency-Sliding Generalized Cross-Correlations Using Convolutional  
599 Neural Networks. ArXiv200200641 Cs Ess.

600 Cox, S.J.D., Scholz, C.H., 1988. Rupture initiation in shear fracture of rocks: an experimental  
601 study. *J. Geophys. Res. Solid Earth* 93, 3307–3320.

602 Engelder, T., 1999. Transitional–tensile fracture propagation: a status report. *J. Struct. Geol.* 21,  
603 1049–1055. [https://doi.org/10.1016/S0191-8141\(99\)00023-1](https://doi.org/10.1016/S0191-8141(99)00023-1)

604 Engelder, T., 1989. Analysis of pinnate joints in the Mount Desert Island granite: Implications  
605 for postintrusion kinematics in the coastal volcanic belt, Maine. *Geology* 17, 564–567.  
606 [https://doi.org/10.1130/0091-7613\(1989\)017<0564:AOPJIT>2.3.CO;2](https://doi.org/10.1130/0091-7613(1989)017<0564:AOPJIT>2.3.CO;2)

607 Favier, N., Chevrot, S., Komatitsch, D., 2004. Near-field influence on shear wave splitting and  
608 travelttime sensitivity kernels. *Geophys. J. Int.* 156, 467–482.  
609 <https://doi.org/10.1111/j.1365-246X.2004.02178.x>

610 Fazio, M., 2017. Dynamic Laboratory Simulations of Fluid-Rock Coupling with Application to  
611 Volcano Seismicity and Unrest (PhD Thesis). University of Portsmouth, School of Earth  
612 and Environmental Sciences.

613 Fazio, M., Benson, P.M., Vinciguerra, S., 2017. On the generation mechanisms of fluid-driven  
614 seismic signals related to volcano-tectonics. *Geophys. Res. Lett.* 44, 734–742.  
615 <https://doi.org/10.1002/2016GL070919>

616 Finck, F., Yamanouchi, M., Reinhardt, H.-W., Grosse, C.U., 2003. Evaluation of mode I failure  
617 of concrete in a splitting test using acoustic emission technique. *Int. J. Fract.* 124, 139–  
618 152. <https://doi.org/10.1023/B:FRAC.0000018234.61956.ff>

619 Frohlich, C., DeShon, H., Stump, B., Hayward, C., Hornbach, M., Walter, J.I., 2016. A historical  
620 review of induced earthquakes in Texas. *Seismol. Res. Lett.* 87, 1022–1038.

621 Hanks, T.C., 1992. Small earthquakes, tectonic forces. *Science* 256, 1430–1432.

622 Hatton, C.G., Main, I.G., Meredith, P.G., 1994. Non-universal scaling of fracture length and  
623 opening displacement. *Nature* 367, 160–162. <https://doi.org/10.1038/367160a0>

624 Healy, D., Jones, R.R., Holdsworth, R.E., 2006. Three-dimensional brittle shear fracturing by  
625 tensile crack interaction. *Nature* 439, 64–67. <https://doi.org/10.1038/nature04346>

626 Heap, M.J., Baud, P., Meredith, P.G., Bell, A.F., Main, I.G., 2009. Time-dependent brittle creep  
627 in Darley Dale sandstone. *J. Geophys. Res. Solid Earth* 114.

628 Huang, L., Baud, P., Cordonnier, B., Renard, F., Liu, L., Wong, T., 2019. Synchrotron X-ray  
629 imaging in 4D: Multiscale failure and compaction localization in triaxially compressed  
630 porous limestone. *Earth Planet. Sci. Lett.* 528, 115831.  
631 <https://doi.org/10.1016/j.epsl.2019.115831>

632 Huang, N.E., Shen, Z., Long, S.R., Wu, M.C., Shih, H.H., Zheng, Q., Yen, N.-C., Tung, C.C.,  
633 Liu, H.H., 1998. The empirical mode decomposition and the Hilbert spectrum for  
634 nonlinear and non-stationary time series analysis. *Proc. R. Soc. Lond. Ser. Math. Phys.*  
635 *Eng. Sci.* 454, 903–995.

636 Hudson, J.A., Kennett, B.L.N., 1981. Quantitative Seismology (two vols) K. Aki and P. G.  
637 Richards, W. H. Freeman, San Francisco 934 pp. \$35.00 ( 20.70 per volume). *Geophys. J.*  
638 *Int.* 64, 802–806. <https://doi.org/10.1093/gji/64.3.802>

639 Kádár, V., Pál, G., Kun, F., 2020. Record statistics of bursts signals the onset of acceleration  
640 towards failure. *Sci. Rep.* 10, 1–12. <https://doi.org/10.1038/s41598-020-59333-4>

641 Kandula, N., Cordonnier, B., Boller, E., Weiss, J., Dysthe, D.K., Renard, F., 2019. Dynamics of  
642 Microscale Precursors During Brittle Compressive Failure in Carrara Marble. *J. Geophys.*  
643 *Res. Solid Earth* 124, 6121–6139. <https://doi.org/10.1029/2019JB017381>

644 Kaneko, Y., Lapusta, N., 2008. Variability of earthquake nucleation in continuum models of  
645 rate-and-state faults and implications for aftershock rates. *J. Geophys. Res. Solid Earth*  
646 113. <https://doi.org/10.1029/2007JB005154>

647 Kato, A., Obara, K., Igarashi, T., Tsuruoka, H., Nakagawa, S., Hirata, N., 2012. Propagation of  
648 slow slip leading up to the 2011 Mw 9.0 Tohoku-Oki earthquake. *Science* 335, 705–708.

649 Kemeny, J.M., Cook, N.G., 1991. Micromechanics of deformation in rocks, in: *Toughening*  
650 *Mechanisms in Quasi-Brittle Materials*. Springer, pp. 155–188.

651 King, T., Benson, P., De Siena, L., Vinciguerra, S., 2020. Acoustic Emission Waveform Picking  
652 with Time Delay Neural Networks During Rock Deformation Laboratory Experiments.  
653 Accepted.

654 Kwiatek, G., Ben-Zion, Y., 2013. Assessment of P and S wave energy radiated from very small  
655 shear-tensile seismic events in a deep South African mine. *J. Geophys. Res. Solid Earth*  
656 118, 3630–3641. <https://doi.org/10.1002/jgrb.50274>

657 Latour, S., Schubnel, A., Nielsen, S., Madariaga, R., Vinciguerra, S., 2013. Characterization of  
658 nucleation during laboratory earthquakes. *Geophys. Res. Lett.* 40, 5064–5069.

659 Lei, X., Kusunose, K., Rao, M.V.M.S., Nishizawa, O., Satoh, T., 2000. Quasi-static fault growth  
660 and cracking in homogeneous brittle rock under triaxial compression using acoustic  
661 emission monitoring. *J. Geophys. Res. Solid Earth* 105, 6127–6139.  
662 <https://doi.org/10.1029/1999JB900385>

663 Lei, X., Nishizawa, O., Kusunose, K., Satoh, T., 1992. Fractal structure of the hypocenter  
664 distributions and focal mechanism solutions of acoustic emission in two granites of  
665 different grain sizes. *J. Phys. Earth* 40, 617–634.

666 Liu, W., Liu, Y., Du, Y., Pang, L., Meng, X., 2019. Study on the Development and Distribution  
667 Rule of Tensile Shear Fracture Propagation Angle of Fractured Rock Mass Under  
668 Seepage Pressure. *Geotech. Geol. Eng.* 37, 4151–4161. [https://doi.org/10.1007/s10706-](https://doi.org/10.1007/s10706-019-00899-w)  
669 [019-00899-w](https://doi.org/10.1007/s10706-019-00899-w)

670 Lockner, D.A., Byerlee, J.D., Kuksenko, V., Ponomarev, A., Sidorin, A., 1992. Observations of  
671 quasistatic fault growth from acoustic emissions, in: *International Geophysics*. Elsevier,  
672 pp. 3–31.

673 Mair, K., Elphick, S., Main, I., 2002. Influence of confining pressure on the mechanical and  
674 structural evolution of laboratory deformation bands. *Geophys. Res. Lett.* 29, 49-1-49–4.

675 McBeck, J., Cooke, M., Madden, E., 2017. Work optimization predicts the evolution of  
676 extensional step overs within anisotropic host rock: Implications for the San Pablo Bay,  
677 CA. *Tectonics* 36, 2630–2646.

678 McBeck, J., Kandula, N., Aiken, J.M., Cordonnier, B., Renard, F., 2019. Isolating the factors that  
679 govern fracture development in rocks throughout dynamic in situ X-ray tomography  
680 experiments. *Geophys. Res. Lett.*

681 McClintock, F.A., 1962. Friction on Griffith cracks in rocks under pressure, in: *Proc. 4th US*  
682 *Nat. Congr. Appl. Mech.* pp. 1015–1022.

683 Mignan, A., 2014. The debate on the prognostic value of earthquake foreshocks: A meta-  
684 analysis. *Sci. Rep.* 4, 4099. <https://doi.org/10.1038/srep04099>

685 Passelegue, F., Nicolas, A., Madonna, C., Schubnel, A., 2016. Influence of the confining  
686 pressure on precursory and rupture processes of Westerly granite. 18, EPSC2016-15867.

687 Passelègue, F.X., Schubnel, A., Nielsen, S., Bhat, H.S., Deldicque, D., Madariaga, R., 2016.  
688 Dynamic rupture processes inferred from laboratory microearthquakes. *J. Geophys. Res.*  
689 *Solid Earth* 121, 4343–4365.

690 Peddinti, V., Chen, G., Manohar, V., Ko, T., Povey, D., Khudanpur, S., 2015. Jhu aspire system:  
691 Robust Ivcsr with tdnns, ivector adaptation and rnn-lms, in: 2015 IEEE Workshop on  
692 Automatic Speech Recognition and Understanding (ASRU). IEEE, pp. 539–546.

693 Ramsey, J.M., Chester, F.M., 2004. Hybrid fracture and the transition from extension fracture to  
694 shear fracture. *Nature* 428, 63–66. <https://doi.org/10.1038/nature02333>

695 Renard, F., McBeck, J., Kandula, N., Cordonnier, B., Meakin, P., Ben-Zion, Y., 2019.  
696 Volumetric and shear processes in crystalline rock approaching faulting. *Proc. Natl.*  
697 *Acad. Sci.* 116, 16234–16239.

698 Schörkhuber, C., Klapuri, A., 2010. Constant-Q transform toolbox for music processing, in: 7th  
699 Sound and Music Computing Conference, Barcelona, Spain. pp. 3–64.

700 Stanchits, S., Vinciguerra, S., Dresen, G., 2006. Ultrasonic Velocities, Acoustic Emission  
701 Characteristics and Crack Damage of Basalt and Granite. *Pure Appl. Geophys.* 163, 975–  
702 994. <https://doi.org/10.1007/s00024-006-0059-5>

703 Tobias, A., 1976. Acoustic-emission source location in two dimensions by an array of three  
704 sensors. *Non-Destr. Test.* 9, 9–12. [https://doi.org/10.1016/0029-1021\(76\)90027-X](https://doi.org/10.1016/0029-1021(76)90027-X)

705 Unakafova, V., Keller, K., 2013. Efficiently measuring complexity on the basis of real-world  
706 data. *Entropy* 15, 4392–4415.

707 Vavryčuk, V., 2005. Focal mechanisms in anisotropic media. *Geophys. J. Int.* 161, 334–346.

708 Waibel, A., Hanazawa, T., Hinton, G., Shikano, K., Lang, K.J., 1995. Phoneme recognition using  
709 time-delay neural networks. *Backpropagation Theory Archit. Appl.* 35–61.

710 Wang, X.-Q., Schubnel, A., Fortin, J., David, E.C., Guéguen, Y., Ge, H.-K., 2012. High  $V_p/V_s$   
711 ratio: Saturated cracks or anisotropy effects? *Geophys. Res. Lett.* 39.

712 Wesnousky, S.G., 2006. Predicting the endpoints of earthquake ruptures. *Nature* 444, 358–360.

713 Yu, M., Wei, C., Niu, L., Li, S., Yu, Y., 2018. Calculation for tensile strength and fracture  
714 toughness of granite with three kinds of grain sizes using three-point-bending test. *PLoS*  
715 *ONE* 13. <https://doi.org/10.1371/journal.pone.0180880>

716 Zang, A., Christian Wagner, F., Stanchits, S., Dresen, G., Andresen, R., Haidekker, M.A., 1998.  
717 Source analysis of acoustic emissions in Aue granite cores under symmetric and  
718 asymmetric compressive loads. *Geophys. J. Int.* 135, 1113–1130.

719 Zang, A., Stephansson, O., 2010. Rock fracture criteria, in: *Stress Field of the Earth's Crust.*  
720 Springer, pp. 37–62.

721 Zhang, J.J., Bentley, L.R., 2003. Pore geometry and elastic moduli in sandstones. *CREWES Res*  
722 *Rep* 115.

723 Zhao, D., Zhang, S., Wang, M., 2019. Microcrack Growth Properties of Granite under Ultrasonic  
724 High-Frequency Excitation [WWW Document]. *Adv. Civ. Eng.*  
725 <https://doi.org/10.1155/2019/3069029>

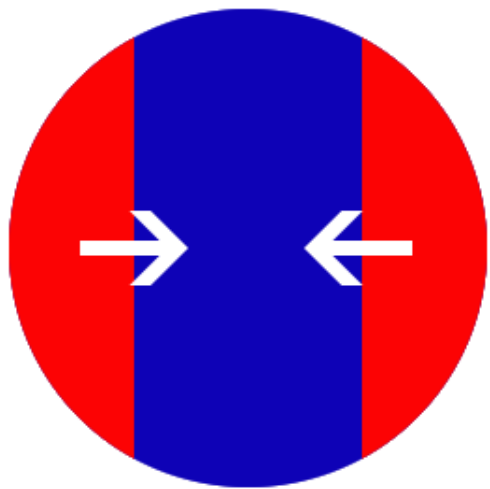
726 Zhu, W., Baud, P., Wong, T., 2010. Micromechanics of cataclastic pore collapse in limestone. *J.*  
727 *Geophys. Res. Solid Earth* 115.

728 Zhu, W., Wong, T., 1997. The transition from brittle faulting to cataclastic flow: Permeability  
729 evolution. *J. Geophys. Res. Solid Earth* 102, 3027–3041.

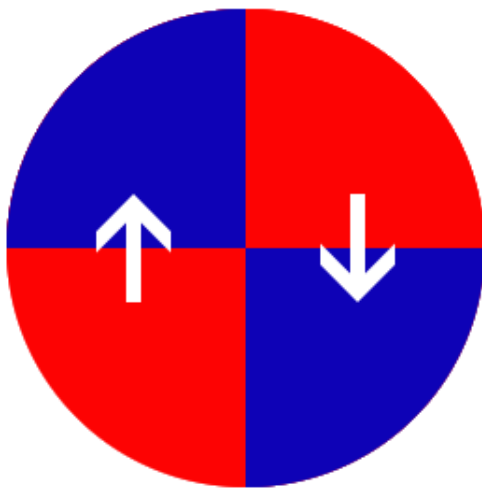
730

Figure 1.

**C-Type**



**S-Type**



**T-Type**

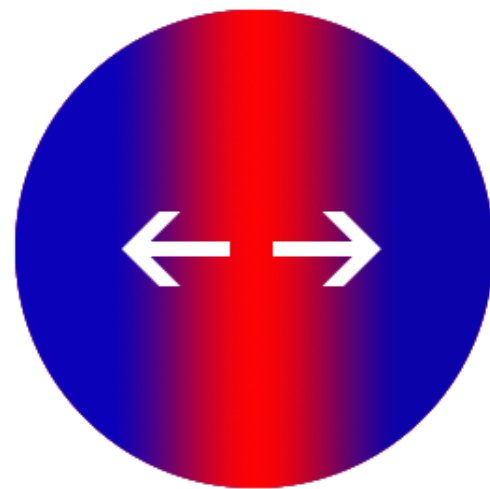
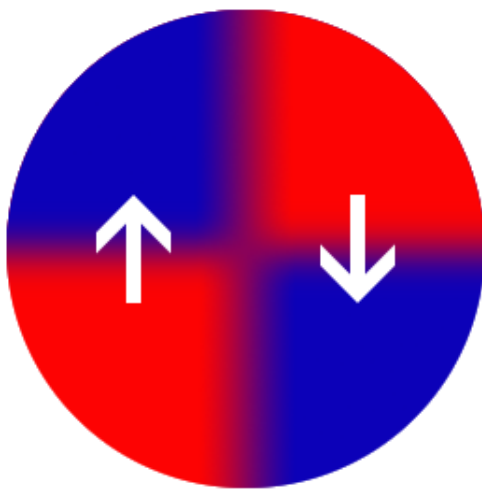
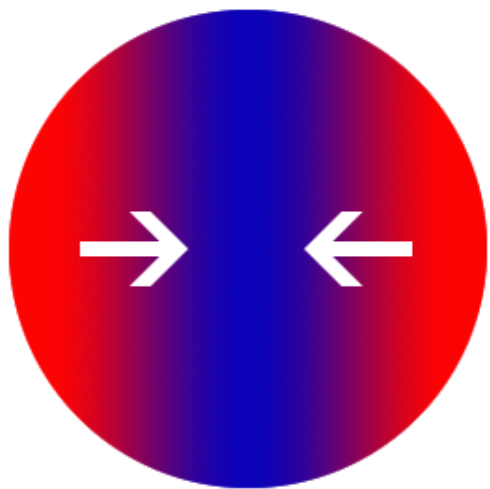
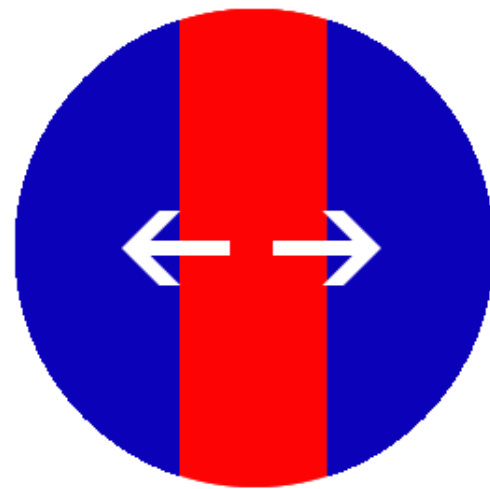
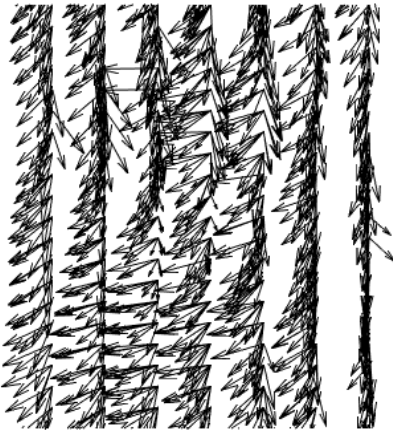


Figure 2.

**Mechanism slip vectors**



**Smoothed interpolation**



**Divergence mapping**

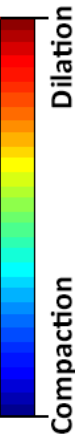
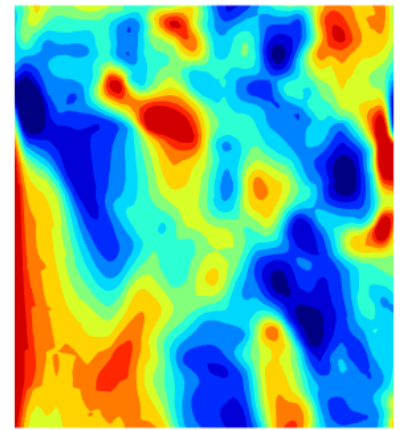
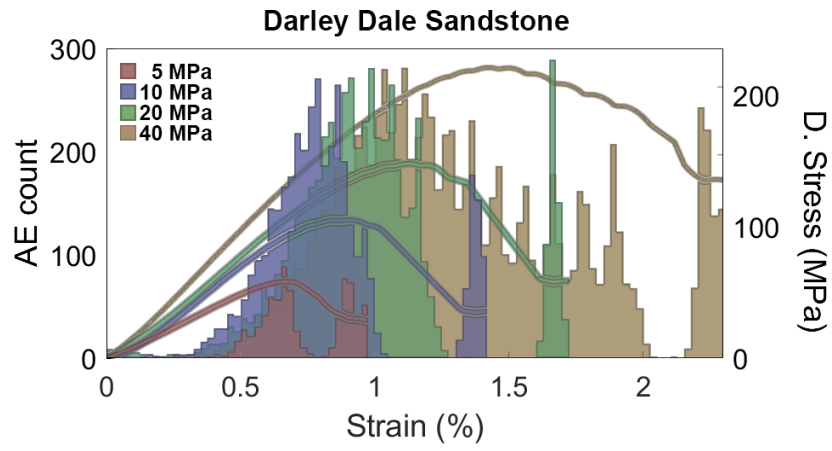
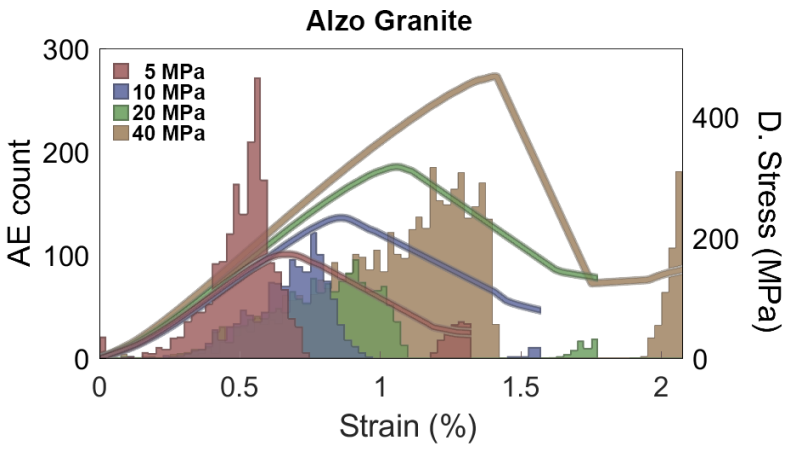
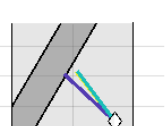
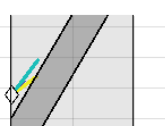
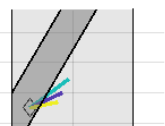
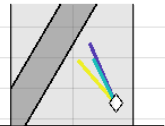


Figure 3.



**Figure 4.**

### Raypaths



2 cm

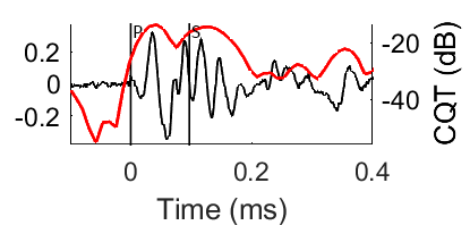
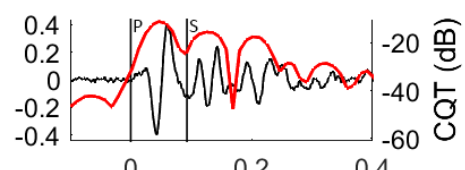
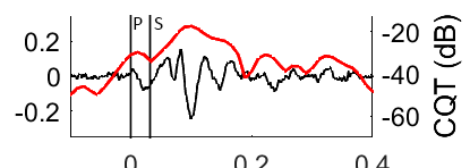
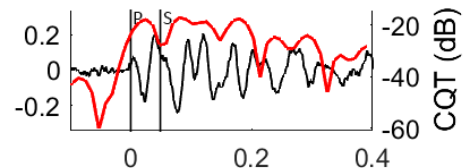
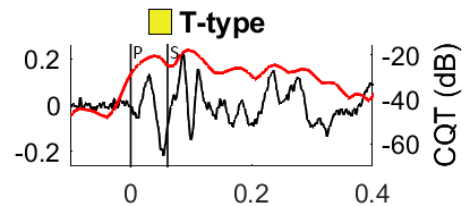
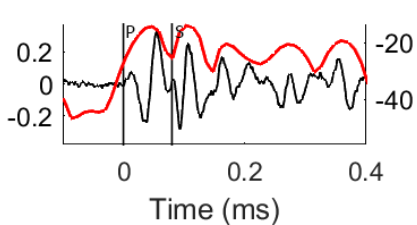
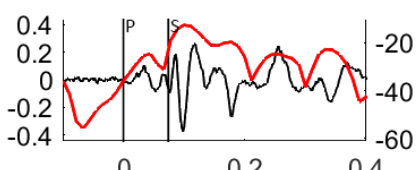
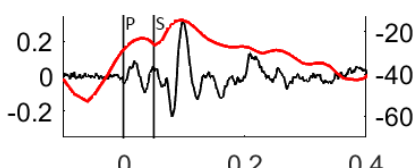
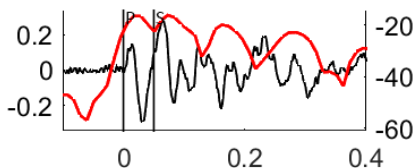
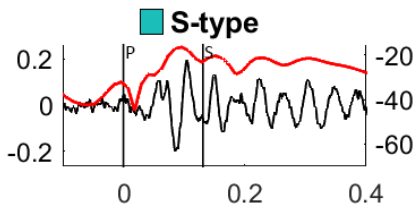
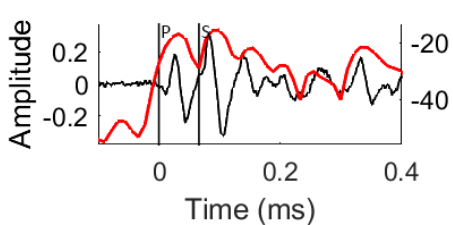
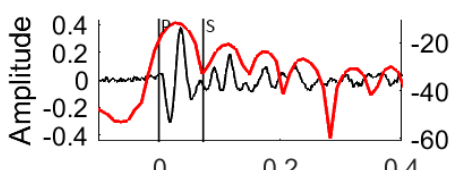
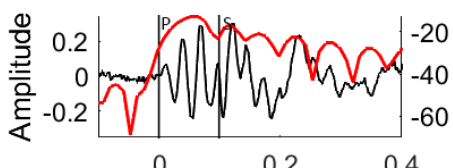
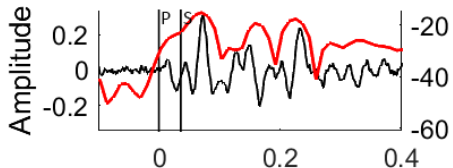
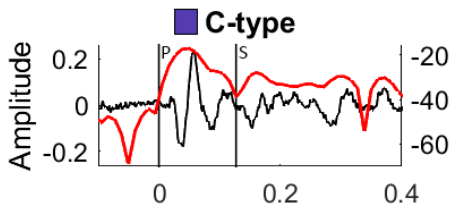


Figure 5.

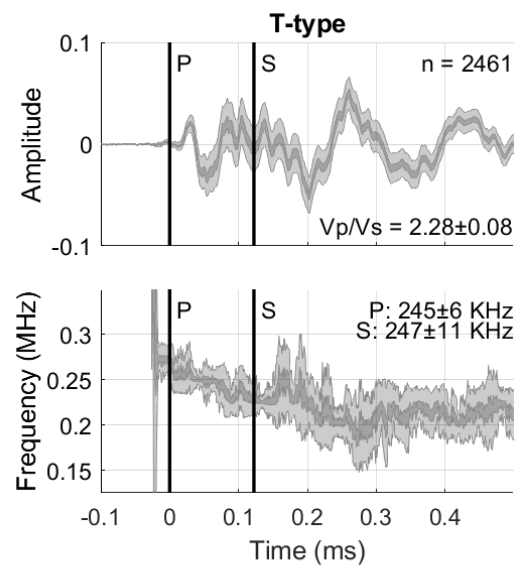
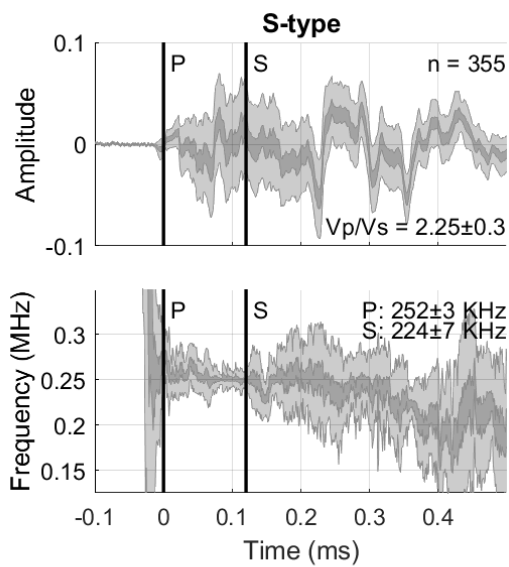
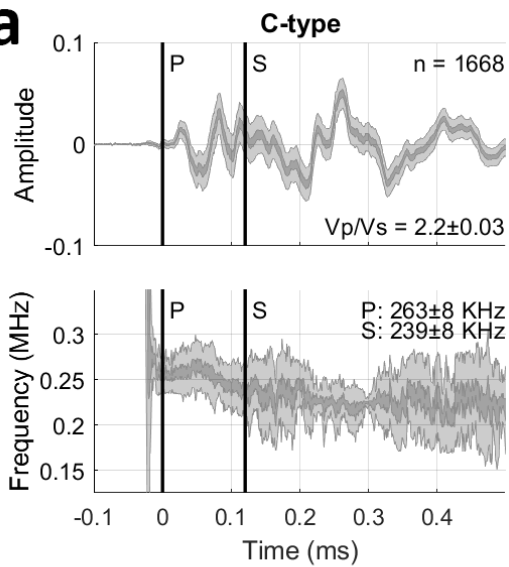
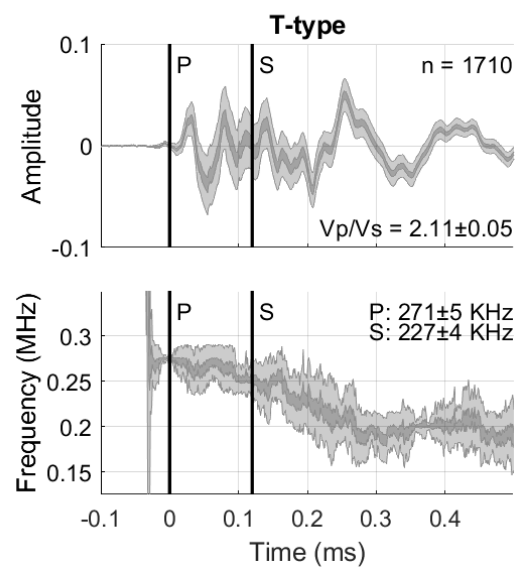
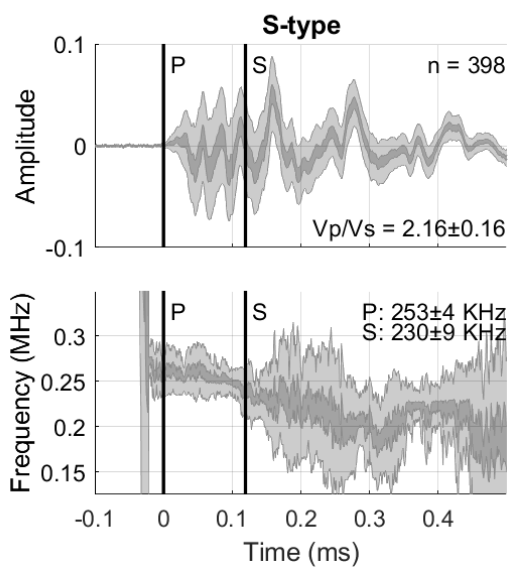
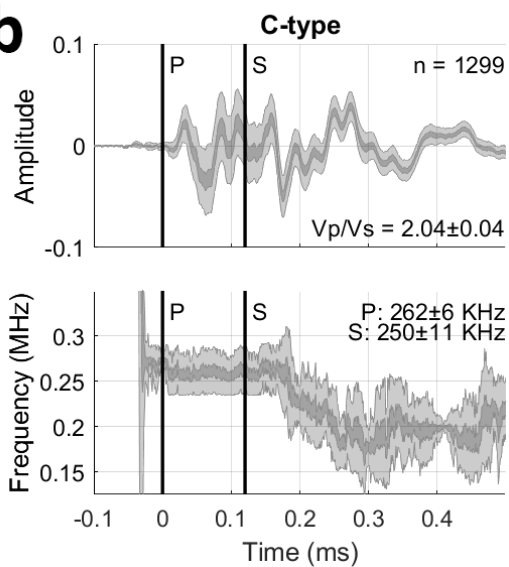
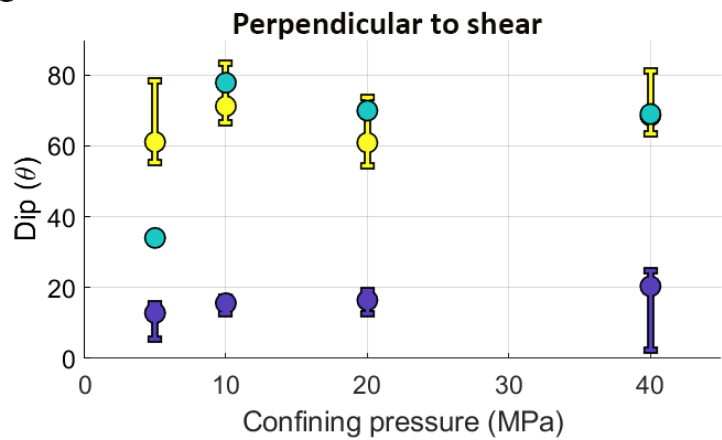
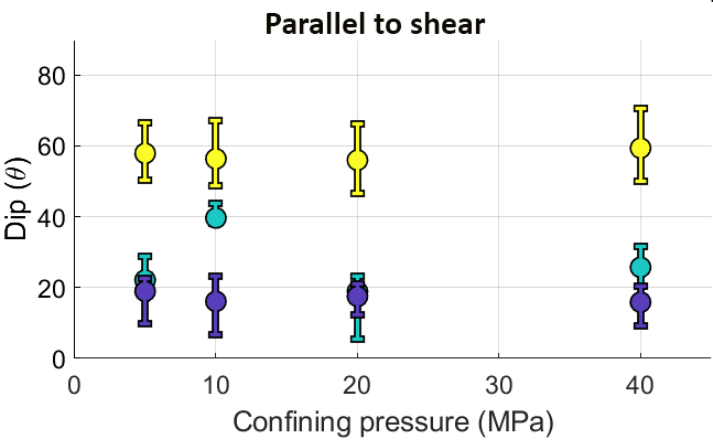
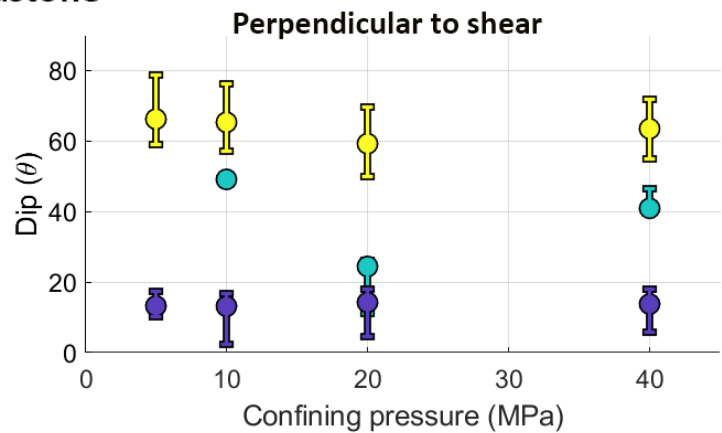
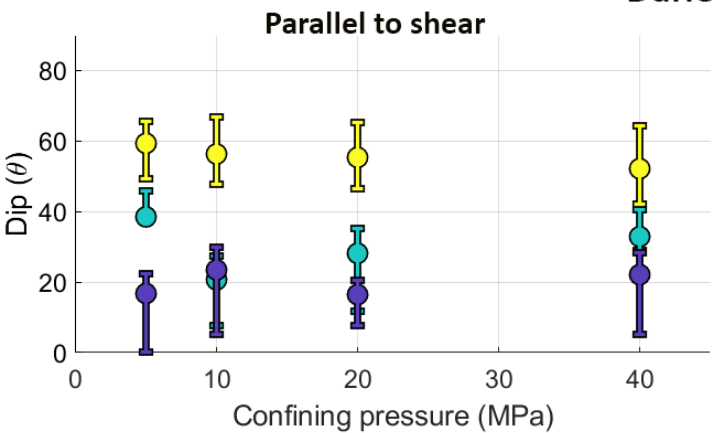
**a****b**

Figure 6.

### Alzo Granite



### Darley Dale Sandstone



**T-type**      **S-type**      **C-type**

Figure 7.

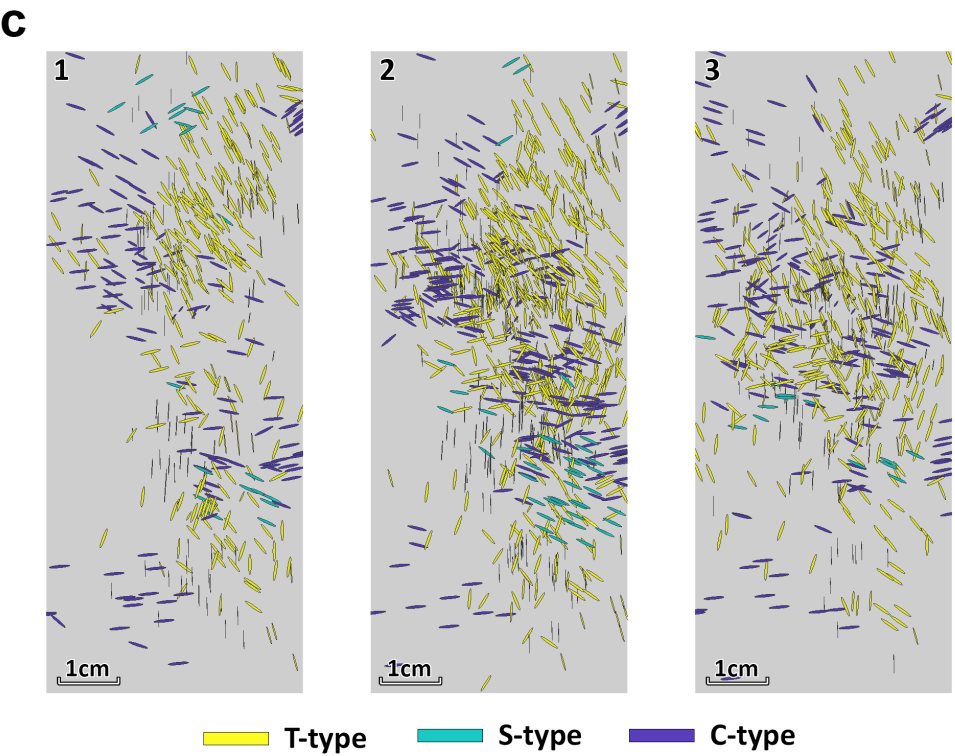
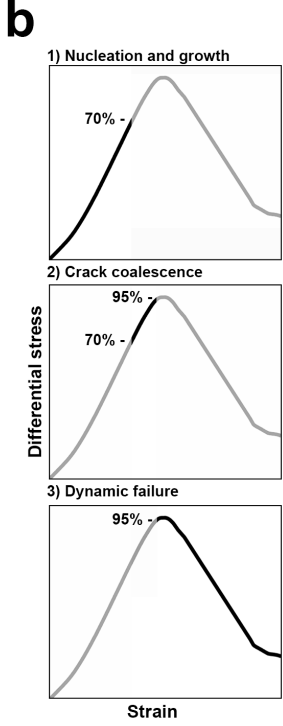


Figure 8.

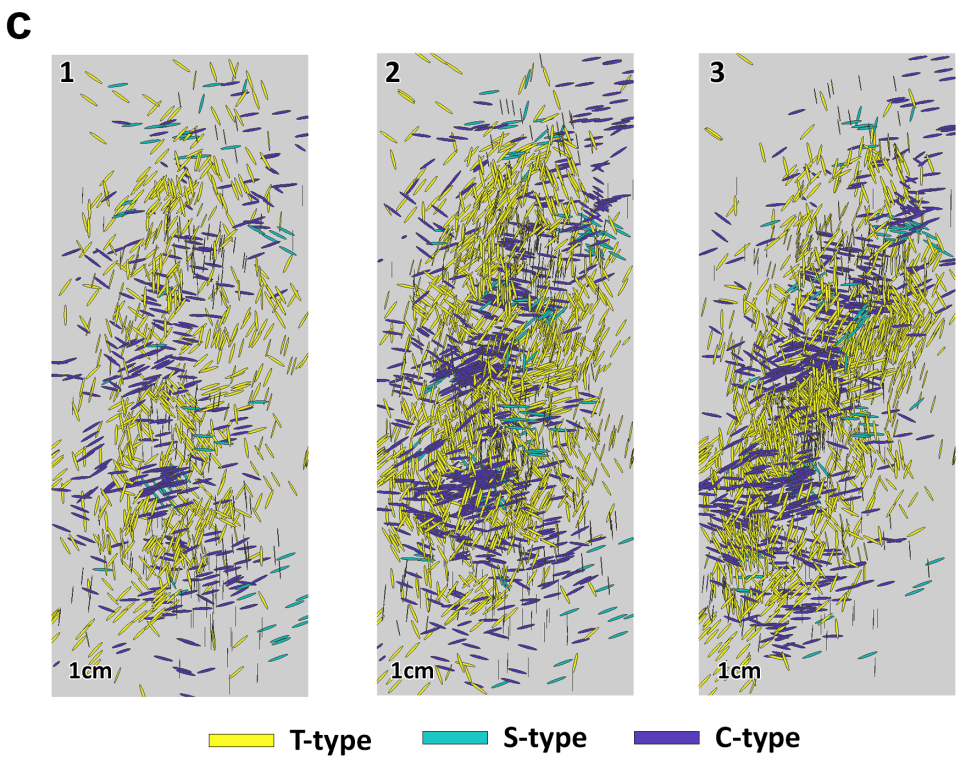
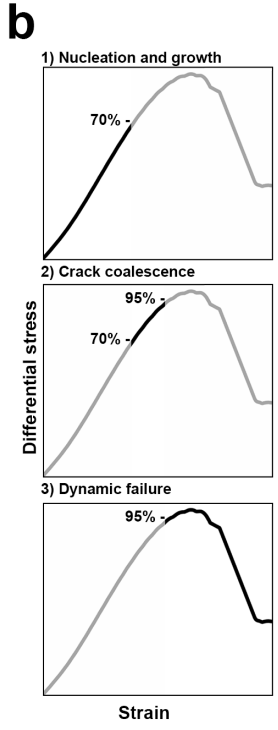
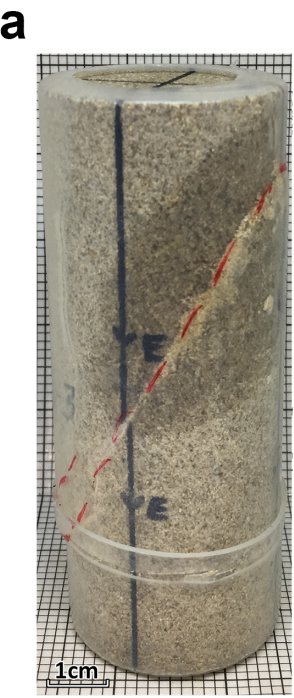


Figure 9.

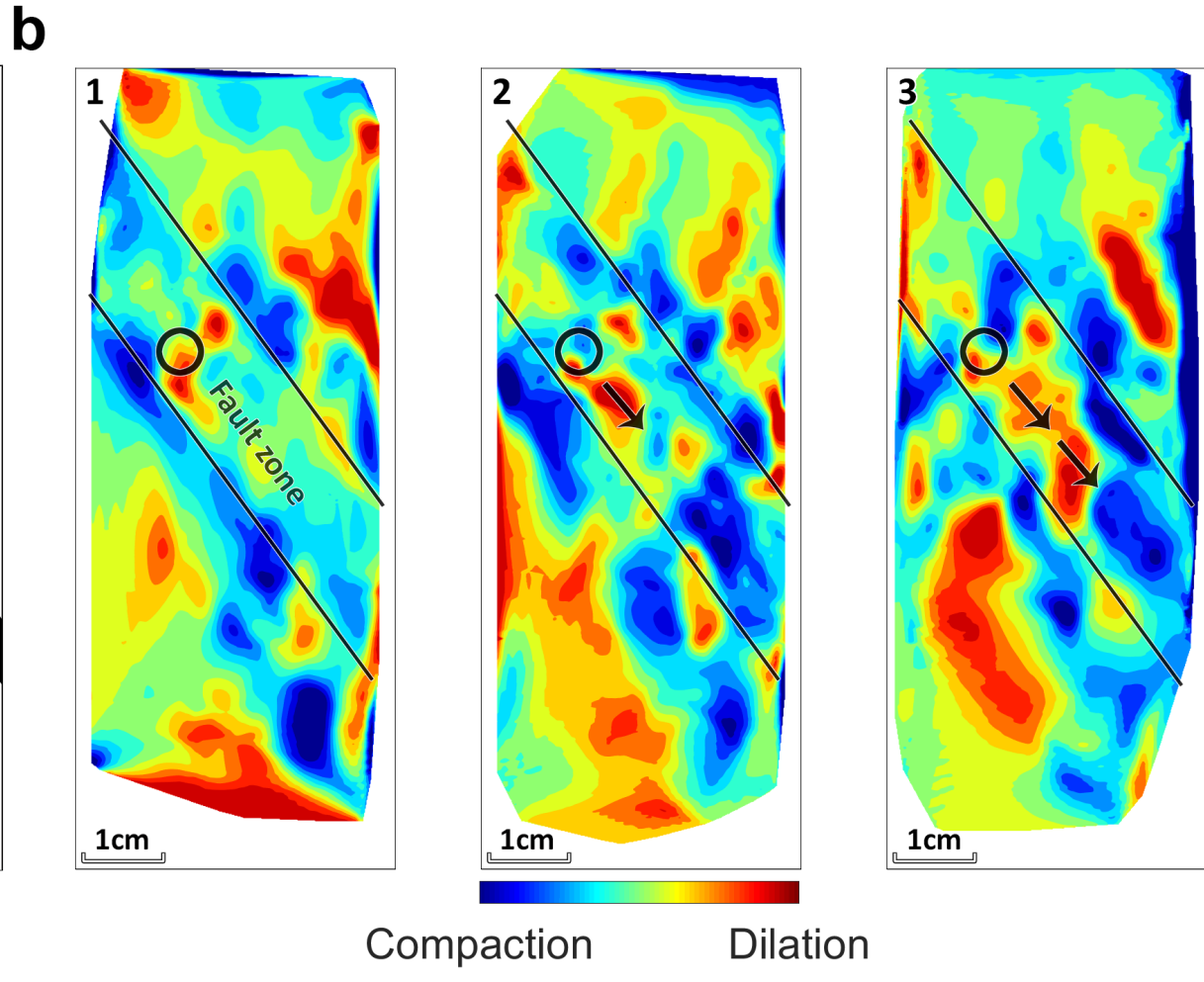
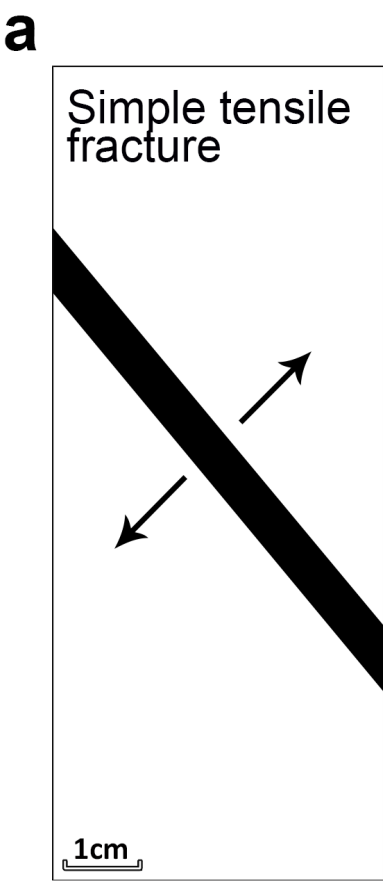
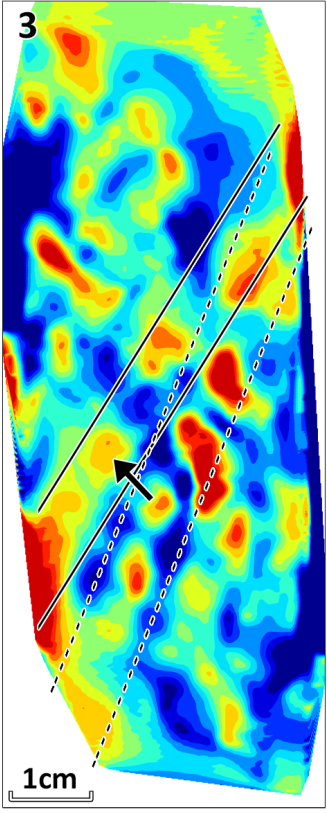
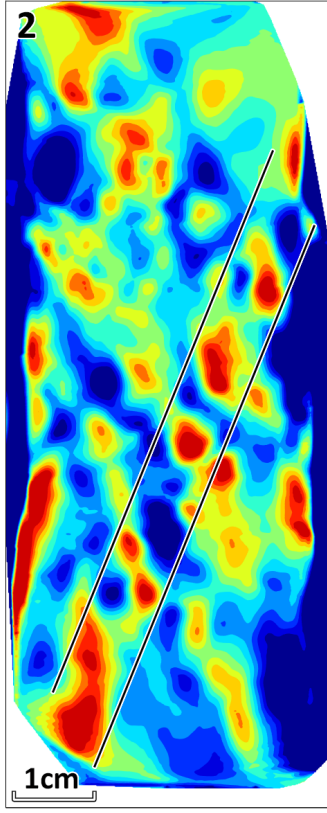
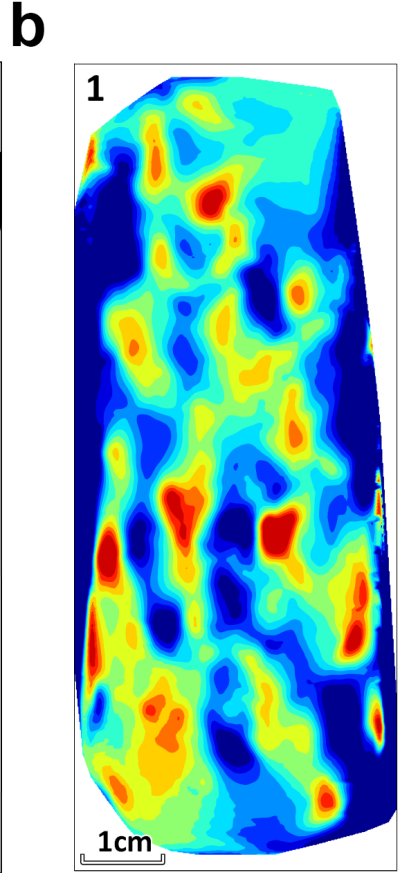
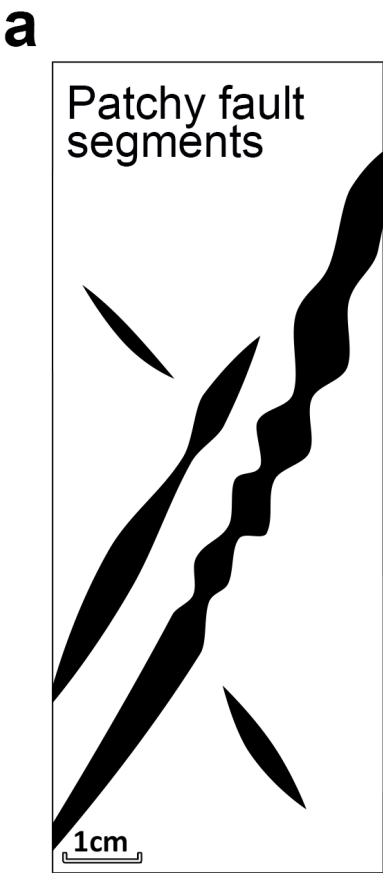


Figure 10.



Compaction      Dilation

Figure 11.

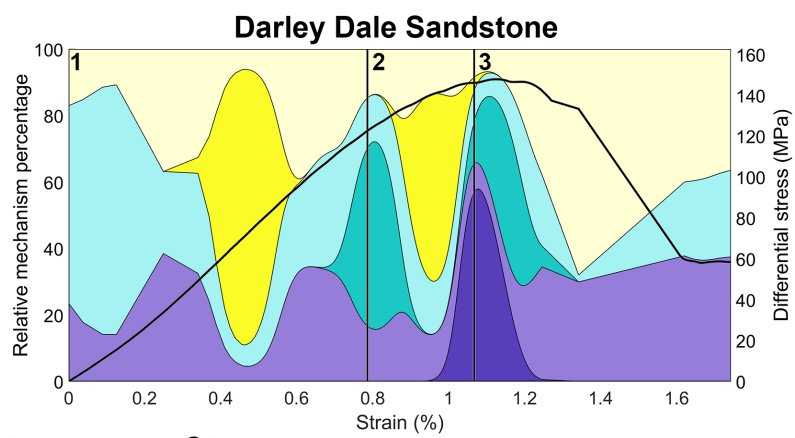
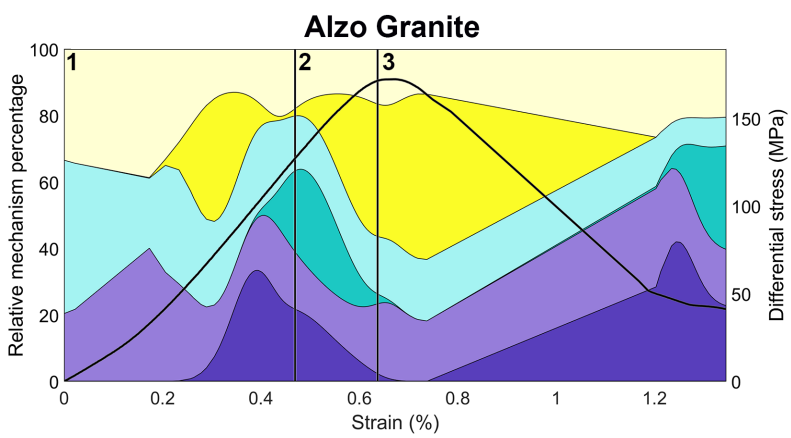


Figure 12.

